Final Report for DARPA Award HR0011-15-2-0003
November 24, 2015

Imaging, Sensing, and Communication Through Highly Scattering Complex Media

Allard Mosk[1], Yaron Silberberg[2], Kevin Webb[3], and Changhuei Yang[4]

[1] University of Twente, Drienerlolaan 5, 7522 NB Enschede, Netherlands: a.p.mosk@utwente.nl
[2] Weizmann Institute of Science, Herzl St 234, Rehovot, 7610001, Israel: yaron.silberberg@weizmann.ac.il
[3] Purdue University, 465 Northwestern Avenue, West Lafayette, IN 47907, USA: webb@purdue.edu
[4] California Institute of Technology, 1200 East California Boulevard, Mail Code 136-93, Pasadena, CA 91125, USA: chyang@caltech.edu

Abstract: Prospects for achievable applications of light in highly scattering media based upon the known physical properties of the media are evaluated, and suggested directions for research and technology are outlined.

Report Documentation Page

Form Approved
OMB No. 0704-0188

1. REPORT DATE	2. REPORT TYPE	3. DATES COVERED
24 NOV 2015		**00-00-2015 to 00-00-2015**

4. TITLE AND SUBTITLE	5a. CONTRACT NUMBER
Imaging, Sensing, And Communication Through Highly Scattering Complex Media	5b. GRANT NUMBER
	5c. PROGRAM ELEMENT NUMBER
6. AUTHOR(S)	5d. PROJECT NUMBER
	5e. TASK NUMBER
	5f. WORK UNIT NUMBER
7. PERFORMING ORGANIZATION NAME(S) AND ADDRESS(ES) **Purdue University, 465 Northwestern Avenue,, ,West Lafayette,,IN, 47907**	8. PERFORMING ORGANIZATION REPORT NUMBER
9. SPONSORING/MONITORING AGENCY NAME(S) AND ADDRESS(ES)	10. SPONSOR/MONITOR'S ACRONYM(S)
	11. SPONSOR/MONITOR'S REPORT NUMBER(S)

12. DISTRIBUTION/AVAILABILITY STATEMENT
Approved for public release; distribution unlimited

13. SUPPLEMENTARY NOTES

14. ABSTRACT
Prospects for achievable applications of light in highly scattering media based upon the known physical properties of the media are evaluated, and suggested directions for research and technology are outlined.

15. SUBJECT TERMS

16. SECURITY CLASSIFICATION OF:			17. LIMITATION OF ABSTRACT	18. NUMBER OF PAGES	19a. NAME OF RESPONSIBLE PERSON
a. REPORT	b. ABSTRACT	c. THIS PAGE			
unclassified	**unclassified**	**unclassified**	**Same as Report (SAR)**	**50**	

Table of Contents

1. Introduction

This report summarizes our collective thoughts on the state of the art in reaching through randomly scattering media with light and the opportunities at this time for substantial impact. The topics covered and the references cited are representative but not exhaustive.

Section 2 describes established understanding methods. Section 3 presents opportunities that stem from recent progress and will applications in new scatter regimes, thereby approaching the physical limits presented. Conclusions are presented in Section 4. Section 5, the Acknowledgement, thanks those who contributed to a workshop held to discuss this field. References are provided in Section 6.

2. Established Concepts Related to Scattering Media

2.1. Introduction - Light in Scattering Media

Light is of key importance in artistic, scientific, medical, industrial, and defense settings because of spectroscopy, information capacity, and the advanced state of source and detector technology. The manipulation of light has evolved from the bronze mirrors of the ancient Pharos of Alexandria to today's optical imaging systems that gather a wealth of information about our environment, our health, and our universe. Optical lithography systems create the essential components of our computers and smartphones, which themselves contain ever more advanced optical systems that acquire and represent information for the user. The almost lossless propagation through transparent media such as air, glass and optical fiber makes light an excellent carrier of information [Gab1946, Cla1962, Pen1983, Bar2008]. However, it remains a challenge to retrieve information from inside turbid materials, such as paint, paper and biological tissue [Ish1978, Seb2001, Tuc2007, Wan2007a, Pop2010b, Boa2012, Wie2013]. In such materials, light is scattered and the information is scrambled. Moreover, materials such as biological tissue are frequently absorbing. Both absorption and scattering extinguish the "ballistic" (straight-propagating) light, and the information it contains, exponentially with depth. However, the presence of scatter can also increase communication capacity because of the presence of multiple, independent channels [Mou2000] and provide security [Pap2002]. The challenge is to decipher the scattered light, or conversely, to be able to control light, and to achieve adequate signal to noise at the detectors.

Many imaging methods have been developed for use in turbid materials. Typically they work by discerning two contributions to the detected light: First, ballistic light that has propagated in a straight line from the lens system to the object or *vice versa*, and second, scattered light whose direction has been changed by scattering one or more times along the way. The ballistic light carries a very high density of information and can be used to make a wavelength-resolution image of the object, provided that the scattered light is rejected. As the intensity of ballistic light decays exponentially with distance in a scattering medium, the signal is insufficient to retrieve an image already at moderate depth.

High-resolution imaging at shallow depth is the domain of multiphoton imaging [Hel2005], which has recently reached depths of about 1 mm in mouse brain tissue, paired with sub-micron resolution [Hor2013]. Multiphoton methods exploit the fact that the intensity of a ballistic optical focus exceeds that of scattered light even at depths of several scattering mean free paths (Box 1). By correcting aberrations in the optical path with adaptive optics techniques, high-resolution imaging can be extended to the limiting depth of the method [Rue2006, Ant2014]. Rapid and label-free imaging at moderate depth is accomplished by gated imaging methods [Abr1978], such as optical coherence tomography (OCT) [Hua1991]. Gated imaging methods selectively detect ballistic light by measuring the travel time of the light pulses with sub-ps accuracy [Wan1991]. OCT offers excellent sub-μm resolution [Dre2001] and high speed [Nas2004]. However, as scatter increases, diffuse light overwhelms the signal, and methods such as OCT fail. An exciting development is the use of wavefront shaping paired with OCT to reach

better image quality and possibly increased depth in a scattering medium [Fio2012, Jan2013]. New developments in ultrafast imaging have given rise to time-gated methods that can capture ultrafast images from wall reflections and potentially inside scattering media [Gup2012, Nai2014]. All of these methods face challenges reaching beyond one transport mean free path (l^*) or thereabouts.

Box 1: Light in turbid materials.

When laser light impinges on a complex material such as paper, paint or skin, it is scattered by nanoscale inhomogeneities such as the fibers in paper, the pigment particles in paint and the cells in skin. Light transmitted through these materials typically follows a long and convoluted path incorporating multiple scattering events, as depicted in panel (a). A small fraction of the incident light continues on a straight path. The intensity of this "ballistic" light decays exponentially with depth, to a very good approximation [Pop2000] following the Beer-Lambert law,

$$I(z) = I_0 e^{-\frac{z}{\ell^*}}, \qquad (1)$$

where $I(z)$ is the intensity of ballistic light at depth z, and ℓ^* is the *scattering mean free path* (also known as attenuation length or inverse scattering coefficient). Small angle scattering perturbs the flow of light less than large angle scattering. The *transport mean free path* (also known as momentum correlation length or inverse reduced scattering coefficient for lossless media) expresses the length over which the angle is completely randomized, and thereby accounts for the average scattering angle [Akk2007, Ntz2010, Boa2012, Sve2013].

As scattering in a solid sample does not perturb the phase coherence of the light, scattered waves that arrive by 'different paths' through the sample show interference. Depending on the detailed positions of the random scatterers, this interference is constructive at some positions and destructive at others. The result is a characteristic pattern of dark and light spots known as laser speckle, shown in (b). This pattern is stable as long as the scatterers inside the sample do not move and the illumination is stable. The average size of a speckle spot is determined by the geometry of the experiment.

The Van Cittert-Zernike theorem [Cit1934, Zer1938, Dai1975, Goo2007] shows that it is similar to the size of the focus of an ideal lens of the same size and distance as the random medium. The total number of spots is approximately equal to the number of degrees of freedom (modes) of the wavefront.

The phase of the light is coherent over an area comparable to a typical speckle spot as shown in panel (c), hence the area of a speckle spot is often indicated as a mode or a coherence area. Many subtle correlations can be found in speckle patterns [Fen1988, Seb2001, Bir2010, Akk2007], and have been exploited for imaging [Fre1990, Put2011, Put2012, Ber2012, Gjo2013, Vel2012, Hsi2010, Kat2014a, Yan2014].

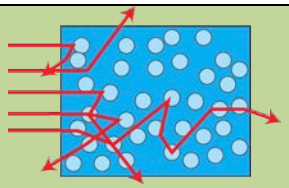

a) Cartoon of the light paths through a strongly scattering medium. Most light is backscattered in the surface layer.

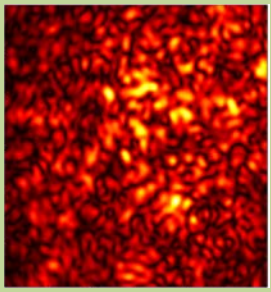

b) Intensity pattern of speckle transmitted through a strongly scattering sample [Akb2013]. True size 10×10 *μm.*

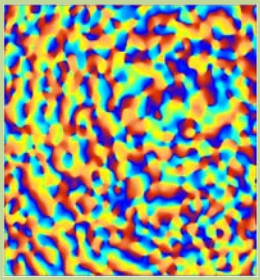

c) Impression of the phase pattern corresponding to (b).

In domains like tissue, turbid water, snow, and aerosols, light is scattered and the information is scrambled. With enough signal to noise, diffusely scattered light can be used to pinpoint the position of a small absorber or source with μm precision [Out1993], and even recover the shape of an embedded object in a collection of methods known as diffuse optical tomography (DOT) or optical diffusion tomography (ODT) [Yod1995, Rey1996, Ye1999a, Ye1999b, Ye2001, Mil2002, Oh2002, Mil2004, Gib2005, Mil2005b, Oh2005, Dur2010, Che2000, Dam2011, Tur2005, Ntz2006, Zac2006]. The resolution has been improved by combining DOT with X-ray or ultrasound tomography [Dur2010]. However, these techniques do not take direct advantage of the coherent nature of scattered light. Coherence plays an essential role in recent work applying wavefront shaping and guidestars to undo scattering, opening prospects for wavelength-scale resolution through substantial scatter.

2.2. Speckle – Coherent Light in Random Media

When coherent light is transmitted through a random medium, the multiple paths available for light propagation give rise to mutual interference and a non-uniform granular light intensity profile on the exit face. The mottled appearance of the transmitted light field is called a speckle light field (Box 1). Speckle has been exploited in many subtle ways. See, for example [Fen1988, Seb2001, Bir2010, Akk2007Fre1990, Put2011, Put2012, Ber2012, Gjo2013, Vel2012, Hsi2010, Kat2014a, Yan2014]. After significant scattering of approximately monochromatic light, and with weakly interacting scatterers, the central limit theorem may define the resulting complex field as a summation of many random phasors. A measurement of polarized light then produces a zero mean circular Gaussian density function. We refer to this type of random optical field as a "fully developed" speckle pattern. On a discretized spatial grid, we may therefore define a fully developed speckle pattern using a circularly complex, Gaussian random variable with zero mean at each grid location. In this case, we can show that the intensity statistics corresponding follow a negative exponential distribution [Web2004]

$$p(I) = \frac{1}{\langle I \rangle} \exp\left(\frac{-I}{\langle I \rangle}\right). \quad (2)$$

The amplitude and phase of the scattered light is correlated over an area comparable to that of a typical speckle spot, and the size can be characterized by the autocorrelation of the speckle intensity pattern. While speckle can be imaged and the size can be controlled by the imaging optics [Web2000, Wan2006], without such steps and with a speckled field over a large spatial support at the scattering medium surface or within the medium, the smallest speckle spot is about λ/2 in diameter, where λ is the wavelength of the light source. When the scatterer's back surface is separated by a distance d from the plane where the speckle is viewed, then the average speckle diameter s takes the approximate value $s = \lambda d/w$, where w is the diameter of the scatterer's back surface. Thus the average speckle size increases linearly with propagation distance d and decreases with the scattering area. The speckle granularity is relevant in our subsequent discussion of the transmission matrix.

A grid qualitatively of size equal to width of a speckle spot has fields that are approximately uncorrelated. Because the field within adjacent grid elements is uncorrelated, the speckle spot area is often referred to as a "speckle mode", or a "coherence area". This speckle spot area is related to the angular distribution profile of the contributing light, and within the scattering medium all possible ray angles are equally present, i.e., the spatial frequency spectrum is approximately constant. The ability to control the field in each speckle mode relates to efficacy of removing the influence of scatter and achieving an optical focus within a scattering medium.

2.3.Tutorial: Transmission Matrix

The granular nature of a speckle field, along with the fact that there is an average speckle size, leads to a very convenient mathematical approach to tackle wavefront shaping. Specifically, we can discretize the input-output relationship of light passing through any random medium, leading to a matrix model for the light's scattering interactions. Consider a random medium with opposing surfaces (faces A and B, the input and output planes, respectively), as shown in Figure 1. For simplicity, we will further assume that the medium is sufficiently turbid so that the speckle field it generates on its back surface is fully developed (i.e., λ/2 in diameter, as noted above). The Nyquist (and Shannon)

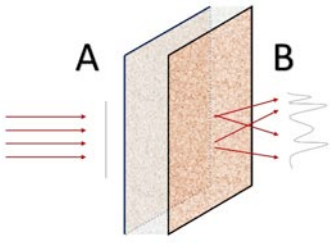

Figure 1: Light transmitted through a scattering medium resulting in a speckle field.

sampling theorem then allows us to fully describe face *A* and face *B* on a discretized sampling grid using a λ/2 sampling period. The light transmission relationship between face *A* and face *B* can be characterized in a matrix representation as

$$E_B = tE_A, \tag{3}$$

where E_A is the complex light field on plane *A* and E_B is the complex light field on plane *B*. Given there are *M* discrete elements in E_A and *N* discrete elements in E_B, we see that E_A and E_B are column vectors containing *M* and *N* elements, respectively. Therefore, we define the (complex, temporal frequency domain) transmission matrix *t* as an *N* x *M* matrix that specifies the relationship between any input field E_A and the resulting output field E_B. For simplicity, we will assume $N < M$. By only considering the light transmitted from face *A* to face *B*, *t* is actually a subset of a more complete transmission matrix that also accounts for any reflection and for light incident from both sides, which we ignore here for simplicity.

It is often very convenient to re-express the transmission matrix *t* using singular value decomposition (SVD)

$$t = U\epsilon V^*. \tag{4}$$

Here, *U* and *V* are (*N* x *N*) and (*M* x *M*) unitary matrices and ε is an *M* x *N* rectangular diagonal matrix with real, non-negative elements along its diagonal. This formulation is useful in gaining insights into the transmission effectiveness of the scattering sample. Matrix *V** maps (i.e., rotates) the incident light from real space coordinates into an orthonormal basis. Each dimension of this new basis represents one of *M* "modes", or "eigenmodes", of light transmission. These scattering modes are in direct analogy with the orthonormal modes of a multimode optical fiber. The diagonal matrix ε assigns a nonnegative scalar weight to each independent scattering transmission mode, and finally *U* rotates the resulting attenuated modes back into real space. If transmission mode *j* is multiplied with a diagonal matrix weight $\varepsilon_{jj} = 1$, then all light through this *j*th mode is fully transmitted from face A to face B.

This particular formulation of the random medium transmission is analogous to the multiple input, multiple output (MIMO) picture of antennas and receivers. Random media in the case of radio antennas and receivers is associated with structures and terrain. One of the most significant MIMO results of practical relevance is the concept of phase optimization for an antenna array. Considering the antenna array as the source of radiation input (side *A*), one can optimize the relative phase of each antenna to maximize the total power delivered to an output detector (on side *B*).

Optimizing for total power transmission is quite different than optimizing for maximum power delivery to a localized area (i.e., a small sub-set of speckles in our situation). As we will discuss later, the maximum deliverable power to a single speckle spot on side *B* scales linearly as function of the number of discrete controllable elements available on side *A*. Box 2 provides additional information regarding transmission modes and the distribution of power within each mode. The interested reader is invited to read this background material for a more detailed mathematical outline of the subject. Briefly, the optimized power in a given channel has been found to be no more than ~2.4 times greater than the amount of power delivered in the non-optimized case [Mar1967, Mou2000, Tul2004]. This result holds true in most optical domain transmission matrix situations as well. While there are certain special cases where the power in one mode can exceed this upper bound [Vel2008a], it is instructive to emphasize that most problems concerning transmission control using wavefront shaping will offer quite limited total transmitted power enhancement. However, the intensity of the focus (power in a given mode) divided by the average of the background (or peak to background (PBR) ratio) is equal to the number of optical modes one controls on the optical control surface. For a typical SLM, this is about 10^6 control variables. Experimentally, ~ 100,000 degrees of freedom in control is currently typical for digital optical phase conjugation, and ~ 1000 for feedback-based wavefront shaping.

Box 2. What is a bimodal distribution?

Can a fully open transmission mode exist in a random medium (with a singular value $\varepsilon = 1$)? The answer turns out to be yes, IF the medium is a waveguide, and the point is illustrated in panels (a)-(c). More generally put, fully open channels exist if the medium does not lose any light, except through faces *A* and *B*. In such a case, the distribution of singular values that define the medium's input-output optical response follow a bimodal distribution, as derived in Refs. [Dor84, Pen92, Bee97]. In this distribution, each singular value is either zero or one (either $\varepsilon_j = 0$ or $\varepsilon_j = 1$). This corresponds to each mode either being "closed" or "open" to transmitting any light. The relative intensity transmitted by scattering mode *j* is given by $T \equiv \varepsilon_j^2$, where ε_j is the *j*th diagonal element of the diagonal matrix ε.

The bimodal distribution of the intensity transmitted by each mode has the form

$$P(T) = \frac{\langle T \rangle}{2T\sqrt{1-T}}, \tag{5}$$

where $\langle T \rangle$ is the average intensity transmittance across all *N* possible channels to the output surface. The probability of unity and zero intensity transmittance is thus

$$\text{Probability}\ (T \sim 1) = \langle T \rangle / N \tag{6a}$$

$$\text{Probability}\ (T \sim 0) = 1 - \langle T \rangle / N \tag{6b}$$

where *N* is the number of optical modes that the scattering media may transmit to side *B*. Therefore, the probability for the channel to be open becomes lower when the scattering media becomes more turbid (i.e., when $\langle T \rangle$ is reduced). The distribution of transmission coefficients for the case of $\langle T \rangle = 0.1$ and 0.01 are shown in Figure 2.

In the analogous radio wave MIMO picture of multiple antennas and receivers, the bimodal distribution will arise when the neighborhood is enclosed within a lossless reflecting medium or can otherwise be viewed as a waveguide. In such a case, a solution exists for antenna transmission where all of the power can make its way say across a city block, albeit through many random reflections off different surfaces.

In a non-waveguide situation, what is the channel distribution?

In the practical case where the light propagation is lossy through the scattering medium, the transmission matrix components become uncorrelated (i.e., the transmission matrix is no longer unitary). In this lossy scenario, the eigenvalue distribution takes the form of a quarter circle distribution [Pop2010, Mar1967]

$$P(T) = \frac{4}{R^2\pi}\sqrt{R^2 - T^2}, 0 \le T \le R, \tag{7}$$

where *R* is $\frac{3\pi}{4}\langle T \rangle$. In this case, the channel with the highest transmission would have a transmission value that is only ~2.36 times higher value than that of the average. The quarter-circle distribution of the transmission coefficients for the case of $\langle T \rangle = 0.1$ and 0.01 are shown in Figure 2.

Most practical situations involving random media belong to this lossy category. We should further note that the loss mechanism does not necessarily have to be leakage-based. Absorption-based loss will also force a random medium to take on a quarter circle eigenvalue distribution.

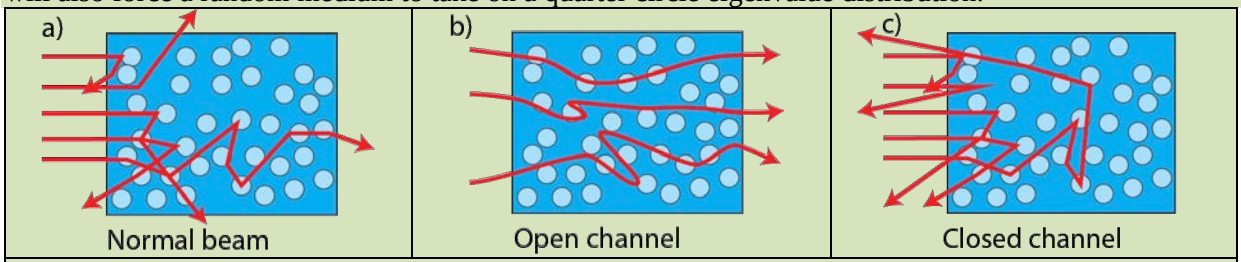

Cartoon of light scattering in transmission channels (a) with a normal (flat wavefront) incident beam most of the light entering a scattering medium is scattered backwards. (b) Light entering an open channel traverses the sample without backscattering to the incident side. (c) Light entering a closed channel is fully backscattered to the incident side.

2.4. Wavefront Shaping Methods

2.4.1. Tutorial: Optimizing for Transmission to a Single Speckle Spot

A large fraction of work done related to wavefront shaping has not aimed to optimize total transmitted power. Instead, the goal of this greater fraction of work was aimed at optimizing power delivery to a single speckle spot. It is worth drawing the distinction. When power delivery to a single spot is optimized for most scattering media (those that obey the quarter circle distribution in their transmission mode distribution), the total power transmitted remains largely unchanged. This type of spot optimization is nevertheless very useful. For example, this would be the case if one has an implant the size of an optical speckle spot in biological tissue at depth L and the goal is to deliver light maximally to that implant. Let' us assume that an area A is illuminated on the skin surface and the resulting speckle at depth L is fully developed. Then, the power delivered to that implant can be boosted by a factor of ~ A/(speckle size) with an optimized wavefront, as compared to the unoptimized case. However, in the total power reaching to depth L will have remained unchanged.

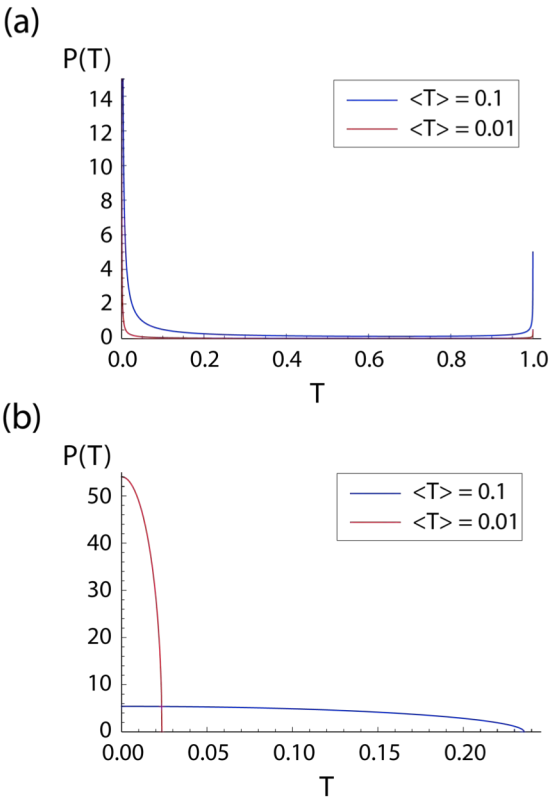

Figure 2: The distribution of the transmission coefficient (eigenvalues) of eigenchannels through disordered media: (a) a waveguide geometry; (b) a lossy configuration.

The correct wavefront desired on side A (given control over M speckle modes/spots), to deliver optimal power to a single speckle spot on side B, is found by adjusting the optical phase front on side A. The goal of such an adjustment is to ensure the contribution of each and every speckle on face A will add *in phase* at one desired speckle location on face B. Suppose that the number of modes on the input and output surface are equal for simplicity ($M = N$), and that the goal is to optimize power delivery to the jth location on side B. Mathematically, the average maximum intensity is given by [Pop2010, Mar1967, and Box 3]

$$\langle I_{max,j} \rangle = \langle I_0 \rangle [(M-1)\pi/4 + 1]. \quad (8)$$

Here, M is the number of scattering transmission modes (i.e., the number of controllable speckles on side A) and $\langle I_0 \rangle$ is the average light intensity in each mode in the un-optimized scenario.

A convenient performance parameter is the peak to (unoptimized) background ratio

$$\text{PBR} = \frac{\langle I_{max} \rangle}{\langle I_0 \rangle} = [(M-1)\pi/4 + 1], \quad (9)$$

which is linearly proportional to the number of controllable modes, M. The derivation of the maximum intensity to background ratio is based on the assumption that the random matrix follows an uncorrelated random Gaussian distribution. Notice that (9) is independent of the scattering medium thickness and the degree of scatter. Provided the transmission matrix can be formed, thickness and scatter are black box parameters that do not impact the PBR.

Box 3: Does the PBR depend on absorptive loss?

For phase only modulation, the spatial light modulator is configured in such a way that all of the output modes constructively interfere. This is also true with the presence of absorptive loss. As both the maximum and the background intensity decrease at the same rate, the ratio of maximum intensity to background remains unchanged.

Is the PBR affected by moving scatterers in the medium (e.g., blood in tissue)?

The maximum light intensity at the target appears when the modulated field compensates for the phase of the elements in the random matrix. This means the phase of the modulated field is phase-conjugated to the associated elements of the transmission matrix. With the presence of moving scattereres, this phase conjugation relationship between the modulated field and the random matrix weakens or vanishes. Therefore, the maximized light intensity at the target reduces and with sufficient motion over the measurement time, the spatial intensity approaches the mean value.

2.4.2. Tutorial: Major Wavefront Shaping Methods

Currently, wavefront-shaping approaches can broadly be categorized into two categories. We summarize the features of each. Box 4 presents some background information.

Category 1 - Adaptive Optimization: In this method, the phase of the light projected by each spatial light modulator (SLM) pixel on side *A* is optimized to maximize the signal at the target spot on the other side of the scattering medium (side *B*). This can be done in a number of ways: (1) By progressively working on the optimization for each pixel, the optimized wavefront shaping solution is found. This method's challenge is that the optimization of the (*N*+1)th pixel after *N* pixels have been optimized requires detecting a small signal change on top of a large established signal. (2) Using blocks of pixels, such as a Hadamard scheme, where the phase is optimized every time for half of the pixels in different geometries, or (3) Using a global optimization algorithm, such as the genetic algorithm, to find an optimal solution. It is not hard to prove that there is always an optimal solution to the problem (that is, the problem is convex), but the underlying challenge remains: Optimization over a large number of pixels is confounded by detection of a small signal over a large signal as *N* increases. In practice, the number of pixels that are used in adaptive optimizations is on the order of ~1000, to obtain an increase in the intensity at the target point by about the same factor, even though SLMs with much larger counts of pixels are available.

Box 4: Shaping waves for imaging and focusing

Spatial wavefront shaping is a technique to control light in disordered media by manipulating the spatial phase of the incoming beam using a spatial light modulator (SLM). In its simplest version, the light at one particular point in or behind the medium is monitored, and an optimization algorithm is applied to maximize the intensity at that point.

In their pioneering work, Vellekoop and Mosk [Vel2007] demonstrated that this procedure can increase the light intensity at the desired point by orders of magnitude, a factor that depends on the number of controllable pixels in the SLM. While still a small fraction of the incident light power, this optimized point can serve as an effective focal point and the basis of several imaging schemes, in particular, when combined with the 'memory effect,' that enables scanning this focus, albeit with a limited spatial range.

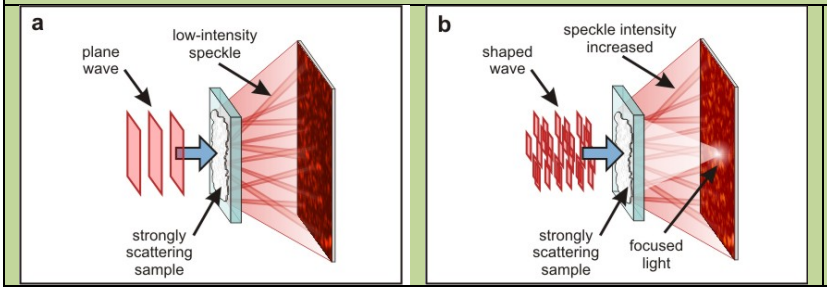

Principle of wavefront shaping: (a) for a plane light wave incident on a strongly scattering sample such as a layer of white paint, the transmitted wave is a low-intensity disordered speckle pattern; (b) a structured wave adapted to the sample is focused to a tight spot.

Category 2 - Optical Phase Conjugation (OPC): In this method, the optimization is done in one shot by the following means. First, light illuminates the target spot on side *B*. The transmission through to side *A* is then interferometrically beaten (heterodyned) with a reference beam and detected by a camera. Through this means, the optimized wavefront solution for side *A* to maximize signal on the target spot is found – it is the phase conjugate version of the detected interference pattern. By imprinting this solution on an SLM that is exactly aligned to the camera, one can generate the requisite optimized wavefront. This approach is technically challenging to implement, as it requires the camera and SLM to be exactingly aligned. However, once aligned, this method yields a very quick optimized wavefront solution. Increasing *N* is also straightforward and does not run into the issue described above for Category 1. In experiments, *N* on the order of 100,000 has been achieved using this approach.

2.4.3. Tutorial: Optical Memory Effect

Imagine a coherent wave illuminating a scattering medium of thickness *L*, and consider the speckle pattern formed on the other side of that medium (Figure 3). Now, if the input wave is tilted by a small angle θ, the first order effect on the speckle pattern is just to shift by θ*L*. If the wavefront has been shaped for focusing in the medium as in Figure 3(b) below, tilting the wave as in Figure 3(c) will shift the focus, an effect that could be used for scanning. The tilt range of the "memory effect" is limited by the speckle correlation length, and it can be estimated for strong scatterer by $\theta_{max} = \frac{\lambda}{2\pi L}$.

Very high-resolution information is present in the intricate speckle correlations in the scattered light [Fre1990]. Recently, a method was demonstrated to image through strongly scattering thin layers using these speckle correlations [Ber2012, Yil2013]. This speckle-scan imaging demonstrates that high-resolution optical imaging is possible even in cases where no ballistic light is present. This non-invasive imaging method has already resulted in several applications [Kat2014a, Jud2013, Yan2014]. Speckle scanning methods rely on the "angular memory effect" in speckle correlations [Fre1990, Li1994, Fen1988], and for a long time such correlations were thought to exist only in very thin scattering media. Recently, it has been shown that these correlations are also present in light reflected by a strongly scattering wall [Kat2012]. Moreover, a new type of speckle correlation, a "positional memory effect" has been discovered that exists in thicker, less strongly scattering materials such as biological tissue [Jud2015]. It is an open question how general this new memory effect is, and whether, as with the angular memory effect, has a range that counter intuitively can be increased by absorption [Ber1989].

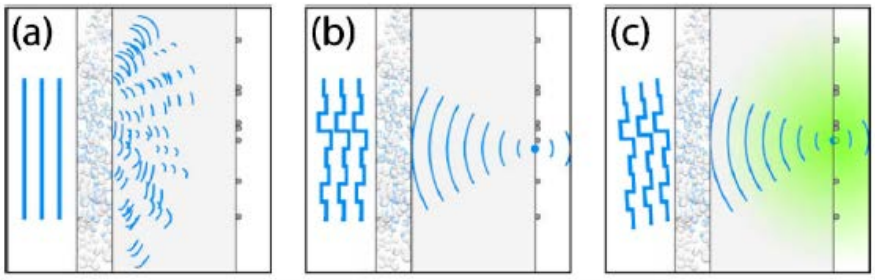

Figure 3: Optical memory effect

2.4.4. Wavefront Shaping Research Status

Spatial wavefront shaping [Vel2007] is a method pioneered by Mosk and coworkers to control light in disordered materials (see Box 2, or for a review of this method and its extensive impact on the field, see [Mos2012]). By optimizing the phase of the incident field in a large number of pixels, one can control the intensity in one or more locations behind the sample [Vel2007, Vel2010a]. Using different

feedback strategies one can create a focus inside the sample [Vel2008b] or even at a specific time [Aul2011, Kat2011, McC2011]. Wavefront shaping has been applied to a variety of imaging and focusing tasks. Optical tweezers have been realized using multiply scattered light and wavefront correction [Ciz2010].

Using correlations in the transmission matrix [Fre1990] or pre-calibrated transmission matrix data, images have been achieved through turbid media [Hsi2010, Pop2010, Yu2013]. Using wavefront shaping, one can even increase the resolution of an image [Par2013]. Wavefront shaping was combined with strongly scattering semiconductor materials to obtain a scattering lens with a record resolution of 97 nm [Put2011].

Wavefront shaping has been used to create a focus through multimode fibers, for optical micromanipulation and imaging [Ciz2011, Cho2012, DiL2011, Mah2013, Pap2013]. The intriguing consequence of this work is that multimode fibers offer high resolution and are physically small, and they offer a good opportunity to realize a "needle endoscope", which is of great medical relevance [Gig2012].

A very interesting development is the use of wavefront shaping for direct imaging using broadband light [Kat2012]. For thin scattering systems, the correlation frequency is broad enough to allow for imaging using filtered thermal light or light from light emitting diodes (LEDs). In addition, wavefront shaping of reflected light has been shown.

Using wavefront shaping, an intriguing effect in scattering media has been elucidated: the existence of open transport channels [Dor1984, Mel1988, Fen1988, Pen1990, Bar1991, Bee1997, Pen2008, Vel2008a]. Light entering such an open channel is transported through the medium without backscattering loss, theoretically even for very thick (but nonabsorbing) media and with strong scatter [Che2014]. Conversely, in a thick medium, the majority of channels are closed: light entering a closed channel is completely backscattered. To enter an open or closed channel, the wavefront of the incident light must match the channel like a lock and key. In nonabsorbing samples, light is fully transmitted (scattered) in open channels. In strongly absorbing materials, there are comparable nonreflective channels in which light is fully absorbed internally [Cho2011]. The exact character of open channels remains an area of active theoretical and experimental investigation [Bei2011, Choi2011a, Ber2005, Pen2008, Shi2012, Dav2012, Kim2012, Goe2013, Yu2013, Hao2014]. Recently, it was found that in partially absorbing materials, light entering open channels is injected deeply and its path is less disturbed by scatter [Lie2014].

2.4.5. Distinction between Adaptive Optics and Wavefront Shaping

We note the distinction between wavefront shaping and adaptive optics. The field of adaptive optics [Har1998, Tys2010] aims to correct aberrations in optical systems, due to, e.g., atmospheric turbulence or refractive index variations [Boo2007, Boo2012]. The correction is typically implemented by a deformable mirror or spatial light modulator [Mau2011], and may be based on models of the disturbance or on model-free measurements. Typical adaptive optics systems efficiently correct for aberrations that takes place in (or near) a specific plane, while the recently developed multi-conjugate adaptive optics can correct aberrations in multiple planes [Tys2010, Sim2013, Boo2012, Boo2014]. The corrections implemented by adaptive optics systems can drastically improve the sharpness of the focus, and therefore the resolution with modest scatter. However, adaptive optics typically uses a small number of degrees of freedom, on the order of 10-100, so that it can correct for aberrations (i.e., weak scatter) but not for scatter (more strongly scattering centers and multiple scatter). Wavefront shaping, in contrast to typical adaptive optics systems, uses up to hundreds of thousands of degrees of freedom to control (multiply) scattered light.

2.5. Guidestars for Control of Coherent Light in Random Media

2.5.1. Tutorial: Concept of Guidestars

One of the most useful things enabled by wavefront shaping is the focusing of light within a random medium. A focused spot of light within a random medium can open up a broad range of biomedically relevant applications, such as targeted optical chemical analysis, precise tissue ablation, and targeted optical activation. To create a focused light spot within a scattering medium requires two conditions: 1) the medium is sufficiently stable that an optimized wavefront solution can be found within the time frame defined by stability, and 2) a guide star of some type at the point of interest within the medium (to provide feedback about the instensity).

A guidestar is simply a way by which the light emerging or transversing the voxel of interest can be tagged or preferentially detected. We operationally define a guidestar as any mechanism that produces an effective source (virtual or real) of sufficiently coherent radiation inside a medium. This could be an actual internal source, such as an emitting molecule, an optical nonlinearity, or a modulation of the local material parameters produced by additional fields, e.g., ultrasound waves. We review the most relevant implementations in the next section.

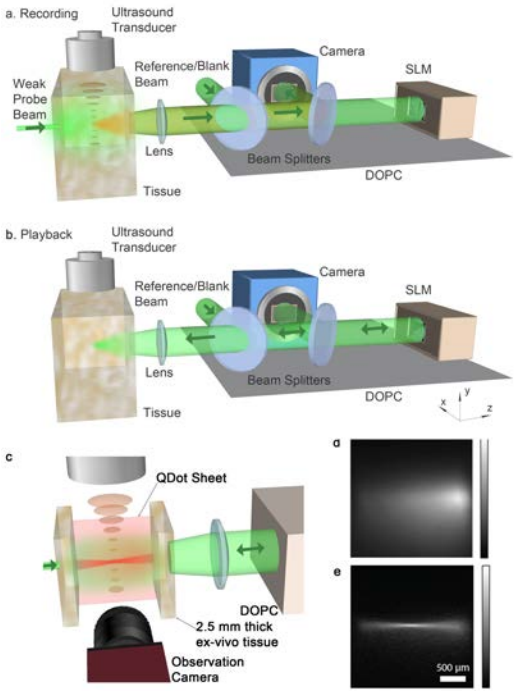

Figure 4: Principles of digital TRUE. (a) Recording: an ultrasound transducer (frequency = f) is used to focus acoustic power into a desired voxel. A weak probe beam is then sent through the tissue. Some of the light passes through the ultrasound focus and is frequency upshifted (by f). By interfering this upshifted component that emerges from the tissue with a reference beam with the DOPC system's camera, its exact wavefront can be characterized. (b) Playback: the conjugated phase map is sent to the spatial light modulator (SLM). A blank beam is then sent to the SLM and reflected off it. By doing this, the SLM will 'imprint' a phase conjugate (or time-reversed) wavefront variation onto the blank beam. This modified beam will then travel back through the sample and come to a focus at the target voxel. (c) Setup for direct visualization of the focusing beam profile. (d) Optical beam profile without TRUE. (e) TRUE focus. Figure d and e reproduced from [Wan2012b], © 2012 NPG.

2.5.2. Guidestar Research Status

One popular and very promising implementation of a guidestar is based on focused ultrasound modulation [Xu2011, Lai2011, Si2012, Jud2013]. This method relies on the acousto-optical effect which frequency-shifts photons that pass through an ultrasound focus. The frequency-shifted photons are then phase conjugated and make their way back to the focus. Lihong Wang's group first demonstrated the use of time reversal for focusing and controlling light *inside* a random medium (tissue) [Lai2011] through the use of ultrasound tagging. By combining the time-reversal property of light propagation with ultrasound tagging, the group achieved a sub-millimeter scale optical focus within a tissue phantom; the technique

was named time-reversal ultrasound encoded (TRUE) focusing [Xux2011]. By moving to an optoelectronic method for implementing OPC (digital OPC), which provides high focusing efficiency, Yang's group demonstrated deep tissue fluorescence imaging with digital TRUE technique (Figure 4) [Wan2012b, Rua2014]. Because ultrasound focus can be flexibly placed at arbitrary positions within a random medium, the TRUE method is so far the only method that allows an optical focus to move freely within random media noninvasively.

Fluorescence was also demonstrated to be a useful guide star candidate for OPC. Vellekoop *et al.* [Vel12] (Yang's group) measured the wavefront from a filtered fluorescent target behind a 0.5 mm thick *ex vivo* chicken breast tissue and sent back the phase-conjugated light. Light was then successfully focused onto the fluorescent target due to the time-reversal symmetry. Specifically, targeting fluorescence with light has a promising future because fluorescence is widely used in the biomedical area as a biomarkers.

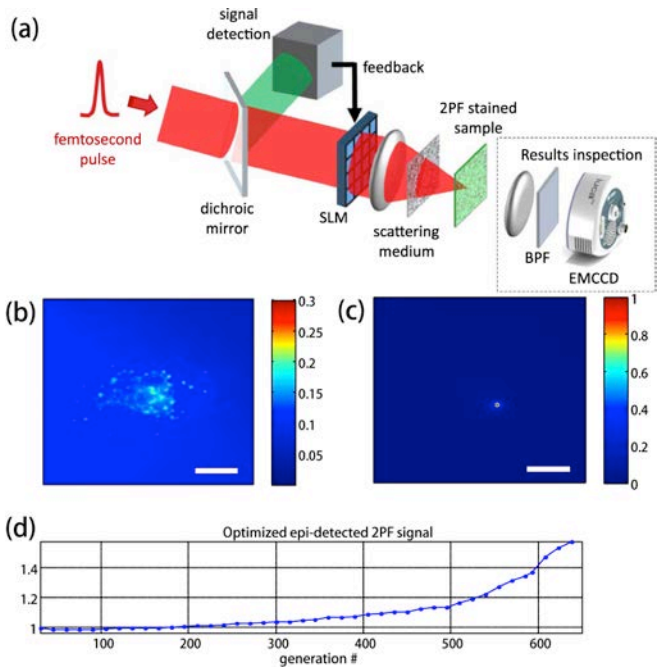

Figure 5: Focusing on a fluorescent sample with iterative optimization. (a) Experiment setup: A spatial light modulator (SLM) is used to shape the incident wavefront based on the feedback from the target. (b) Image of the sample plane without optimization. (c) Optimized focus. (d) Fluorescent signal enhancement over generations of the genetic algorithm. Figure reproduced from [Kat2014b], © 2014 OSA.

In order to focus light using multiple output modes or at arbitrary points, the (field) transmission matrix of the scattering medium needs to be measured. With full knowledge of the transmission matrix, communication with coherent light through great amounts of scatter is in principle possible. Transmission matrix measurement of 0.5 mm thick chicken tissue was demonstrated [Cha2013] using photoacoustic signals from multiple optical absorption objects as feedback. Using red blood cells as the photoacoustic source, this method has potential for light delivery to biological tissues noninvasively. In contrast to using endogenous guide stars, it is also possible to create virtual guide stars between the scattering layers by using ultrasound to modulate scattered light within the tissue to map out the transmission matrix over a limited area [Jud2013] (Yang's group). The method, termed Time-Reversed Optical Variance-Encoded light (TROVE), can identify a single optical mode within the ultrasound profile, which typically contains hundreds of optical modes. Ultrasound-modulated light with various realizations of the incident speckle field was sampled, and shifting and weighting the ultrasound profile uniquely encoded the positions of the optical modes within the ultrasound profile. Analyzing the variance of the ultrasound modulated light intensity can then isolate these optical modes. Therefore, this method essentially measures the transmission matrix of the scattering layers. Compared to the previous transmission matrix measurement method, TROVE allows the light focus to be steered arbitrary within a certain depth. TROVE also has potential for light focusing within the tissue, as does a previous time-reversed ultrasonically encoded (TRUE) light technique (Figure 4) [Wan2012b]. The approach offers fast beam steering and high resolution, but the measurement of the transmission matrix is slow and likely to be impractical for *in vivo* tissue and other rapidly changing random media applications.

There are other methods for implementing a guide star within a random medium for optical focusing purposes. One such technique is termed Time Reversal by Analysis of Changing wavefronts

from Kinetic targets (TRACK) [Zho2014a] (also called time-reversed adapted-perturbation (TRAP) in a separate, independent work [Ma2014]). This method measures two optical fields with a target point scatterer at two different locations in the random medium. By taking the difference between two fields (background subtraction), this method essentially extracts the field scattered only from the moving target. By playing back an optical phase conjugate copy of the difference light field, the OPC field is then able to create an optical focus at the target's location.

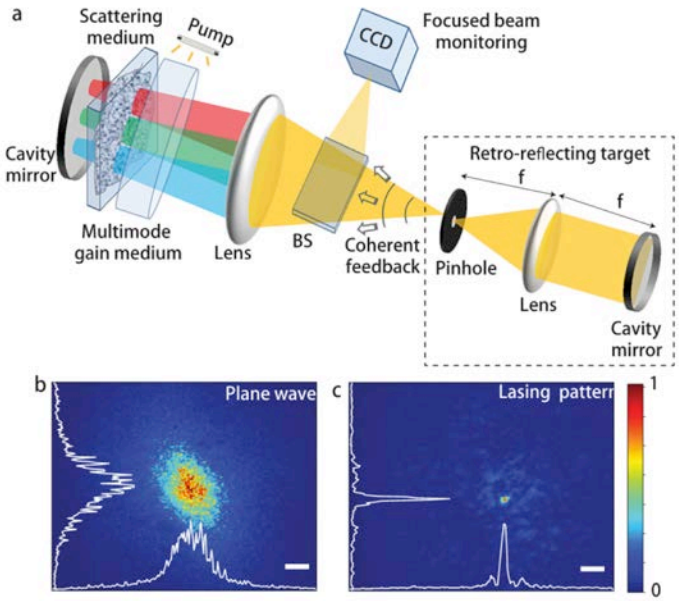

Figure 6: Wavefront shaping through scattering media by all-optical feedback. (a) Experimental setup: a scattering sample is placed inside a degenerate self-imaging 4f cavity. A pinhole placed at the centre of the cavity serves as the target for light focusing, ensuring that only focused components of the light are fed back to the gain medium. (b) Intensity distribution at the target plane for conventional focusing of a plane wave from an external source through a 200-mm-thick slice of chicken breast. (c) Intensity distribution at the target plane for the lasing pattern, demonstrating sharp focusing of the light through the scattering sample on the target. Scale bars, 1 mm. Figure reproduced from [Nix2013], © 2013 NPG.

Although the OPC technique generally involves a two-step process (wavefront recording and playback), its focusing speed is high enough (~100 ms) for some biological applications where tissues can be properly immobilized. Cui *et al.* [Cui2010b] experimentally obtained light focus through a pinched rabbit ear *in vivo*. Recently, Jang *et al.* [Jan2015] successfully created a light focus through immobilized live mouse dorsal skin flab and characterized the relationship between light intensity decay at the focus and tissue decorrelation. These experiments provide evidences that the OPC technique has significant potential for focusing light within biological tissue *in vivo*. The approach provides fast wavefront optimization for a single point but requires coherent or partially coherent guide star sources.

Yet another way to implement a guidestar uses a fluorescent target. The Mosk group showed that by adjusting the optical wavefront of the excitation light to maximize fluorescence from a turbid sample, it is possible to focus light onto the fluorescent target [Vel2008b]. The effectiveness of the focus can be enhanced by using nonlinear feedback such as two-photon fluorescence and optimizing the *total fluorescence* as measured back through the scattering layer (Figure 5). Combined with the memory effect, a scanned image of the fluorescence object could be obtained [Kat2014a]. Nonlinear feedback also ensures that wavefront shaping of short pulses will result in compressed pulses at the focus [Kat2011], important for nonlinear microscopy modalities. This class of guidestar approach is all-optical in nature.

Although the SLM dominates wavefront shaping devices, its operation speed is one of the major hurdles for it to be widely used in applications associated with tissue *in vivo*. Nixon *et al.* [Nix2013] recently reported an all-optical feedback method based on an optical focusing technique that was able to focus light through a 200 micrometer chicken breast sample on a sub-microsecond timescale (Figure 6). This approach relies on a field self-organization process within a multimode laser cavity in which the lasing process naturally selects the lasing state with minimal loss. Although the retro-reflecting configuration, which is needed for lasing, is difficult to adapt to focus light inside biological tissue noninvasively, this method provides opportunities for high speed wavefront shaping.

One of the main difficulties in wavefront shaping is the need to measure the light distribution in the region where we want to optimize it, as this could be inside the medium or behind it in a region that may not be accessible. One solution is to insert a 'guide star", a reporter that will localized at the desired focal point and will, for example, fluoresce or otherwise send a signal proportional to the light intensity at that location, but this of course is invasive. It is possible, however, to optimize the wavefront non-invasively, when the medium responds in a nonlinear way, for example when it is *n*-photon fluorescence (and therefore the fluorescence intensity grows as $I(r)^n$) . In that case, the total integrated fluorescence from the *entire* sample will grow if the light is focused, and then it is possible to form a focus by optimizing the total fluorescence without observing the focal region directly. This should work in any sample when $n>2$, however, in the case of $n=2$, that is the common case of two-photon fluorescence, optimization of total fluorescence will be effective only for thin fluorescence layers (or in sparsely fluorescence specimens).

2.6. Tutorial: The Diffusion Model

Under restricted scatterer densities that will hold in most practical situations, and the assumption that scatter dominates absorption, the diffusion equation describes the mean intensity with sufficiently heavy scatter. In this way, the geometry of the scattering medium in relation to the sources and detectors can be considered.

The diffusion equation in the time domain can be written as

$$\frac{1}{c}\frac{\partial}{\partial t}\phi(r,t) - D\nabla^2\phi(r,t) + \mu_a\phi(r,t) = S(r,t), \tag{10}$$

where c is the speed of light in the medium, D is the diffusion coefficient given by $D = \{3[\mu_a + (1-g)\mu_s]\}^{-1}$, μ_a is the absorption coefficient, $\mu_s' = (1-g)\mu_s$ is the reduced scattering coefficient, with μ_s the scattering coefficient and g is the mean cosine of the scattering angle. $S(r,t)$ is the photon source, and for an isotropic point source at the origin, it is equivalent to $\delta(0,0)$.

The solution to (10) in an infinite homogenous medium is given by the Green's function

$$\phi(r,t) = c(4\pi Dct)^{-3/2}\, exp\left(-\frac{r^2}{4Dct} - \mu_a ct\right). \tag{11}$$

The photon current density can then be calculated from Fick's law, where

$$J(r,t) = -D\nabla_r\phi(r,t), \tag{12}$$

which gives

$$J(r,t) = \frac{r}{16(\pi Dc)^{3/2}}(t^{-5/2})exp\left(-\frac{r^2}{4Dct} - \mu_a ct\right). \tag{13}$$

Normalizing the current density at a position r_o gives the temporal path length distribution $p(t)$ as

$$p(t) = \frac{J(r_o,t)}{\int J(r_o,t)dt}. \tag{14}$$

Because $p(t)$ does not have a simple analytical solution, we show a plot of a numerical solution in Figure 7. This result gives the path length distribution from a point source at the origin to points on the surface of a sphere with a radius of 100 mm. From the expected value of t we can estimate the mean path length as

$$\langle l\rangle = c\langle t\rangle, \tag{15}$$

where $\langle t \rangle$ is the expected time for a photon to travel a distance r from the origin. Additionally, the coherence length can be estimated from the standard deviation of t, σ_t, as

$$\sigma_l = c \cdot \sigma_t. \tag{16}$$

We see that the expected value and standard deviation of t do not depend on the normalization in (14). Thus, (13) can be used to estimate the coherence length requirement for light, as well as the mean path length and the spread (where the spread relates to source coherence requirements). For example, we see that if r is increased in (13), both the coherence length and the mean free path will increase, as expected. Another estimate for the mean path length can be obtained from (13) by assuming $\mu_a = 0$, $l^* = 4D$, $l = ct$, and solving for l when the exponential decay reaches the e^{-1} point. This results in

$$l = r^2/l^*. \tag{17}$$

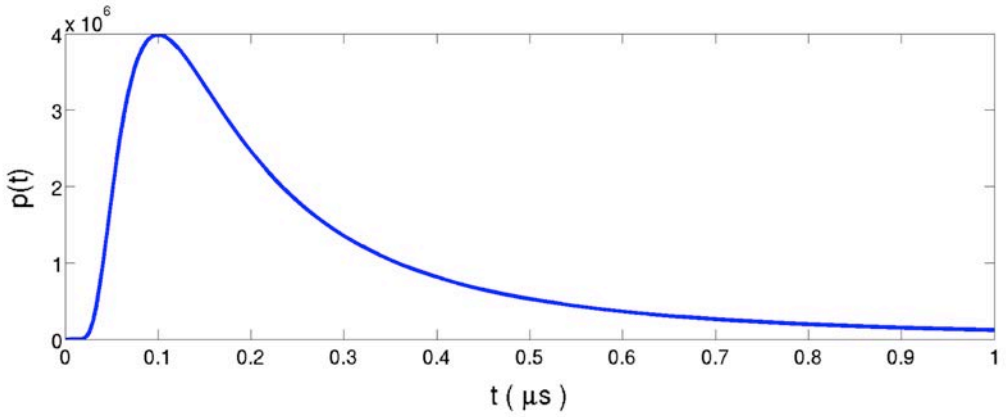

Figure 7: Plot of $\boldsymbol{p(t)}$ in (9) using $\mathbf{c = 3{\times}10^8}$ m/s, $\boldsymbol{\mu_a = 0}$, $\boldsymbol{\mu_s' = 10}$ mm-1, and $\boldsymbol{r = 100}$ mm. The integral of $\boldsymbol{p(t)}$ over the time scale is 1, as expected for a probability distribution. The expected value $\boldsymbol{\langle t \rangle}$ of $\boldsymbol{t}$ is 0.261 **μ**s and the standard deviation $\boldsymbol{\sigma_t}$ of $\boldsymbol{t}$ is 0.201 **μ**s. Using equations (15) and (16), the mean free path is 78 m and the coherence length is 60 m.

2.6.1. Diffuse Optical Tomography (DOT or ODT)

With a model for the scatter, for example, the diffusion equation given in (10), image and sensory information for objects in the scattering medium can be obtained. The recovery of the shape of an embedded object or the reconstruction of the scattering and absorption parameters (μ_s' and μ_a) is known as diffuse optical tomography (ODT) [Ye1999a, Ye1999b, Ye2001, Oh2005] and also diffuse optical tomography [Arr1999, Dur2004]. ODT has proven to be a powerful modality and applied successfully in biomedical imaging [Boa2001], such as the study of breast cancer [Bov2007, Fan2008]. An important application of ODT is the imaging of fluorophores that are coupled with cancer targeting agents [Bal1997, Bec2001,Mil2004, Ntz2006]. An example ODT reconstruction of 3D printed mice is shown in Figure 8.

In frequency-domain fluorescence ODT (FODT), sinusoidally modulated light at the fluorophore's excitation wavelength λ_x is launched into the tissue. When the excited fluorophores decay to the ground state, they emit light at a longer (emission) wavelength λ_m, and this emission is measured by an array of detection devices. These emission data are used to perform a volumetric reconstruction of the yield (a measure of the fluorescence efficiency) and the lifetime (the fluorescent decay parameter). The

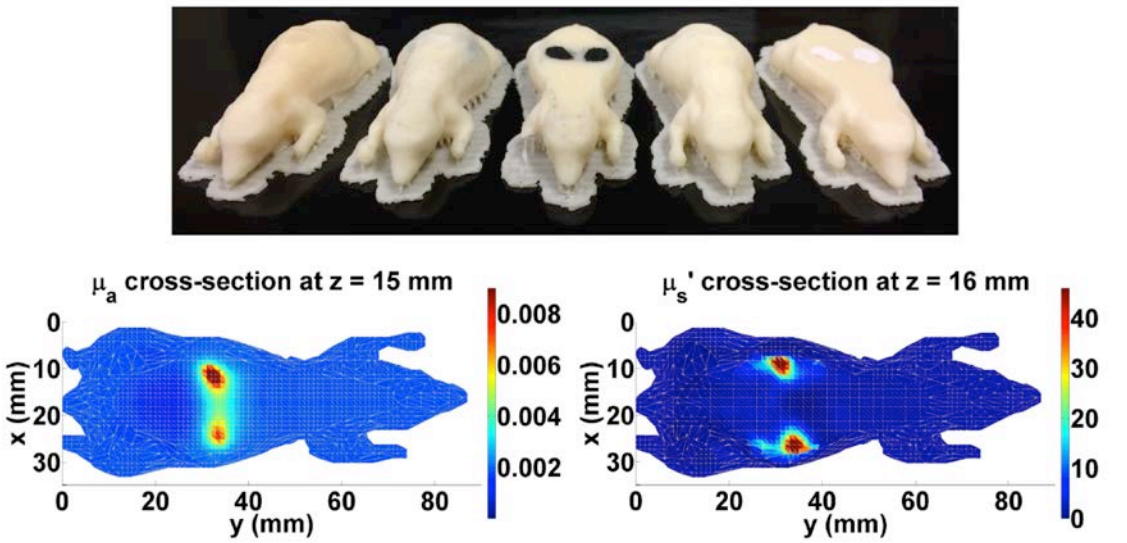

Figure 8: 3D printed phantoms with inhomogeneities in the shape of the kidneys (top). Experimental data captured form the mouse second to the right (with highly scattering inhomogeneities) was used for an ODT reconstruction of the absorption and scatter parameters. The results of this reconstruction are shown (bottom) [Ben2015].

task in FODT is to determine the image from an appropriate measurement set. FODT can further be applied to image Fluorescence (or Förster) resonance energy transfer (FRET) [För1948, Gai2009, Gai2010]. FRET is a non-radiative energy transfer process between donor and acceptor (DA) fluorophores spatially separated by a distance usually between 1-10 nm that can provide invaluable information for nanomedicine. For example, in vitro FRET applications have shown the FRET distance (the distance between DA molecules) can be used as an indicator of molecular activity [Tru2001]. With ODT, it is possible to image FRET parameters, including the nanoscale DA distance [Gai2009, Gai2010], in a method called FRET-ODT.

ODT (or DOT) has recently seen a major advance in spatial resolution through the so called high density diffuse optical tomography (HD-DOT) methods [Zef2007,Whi2010]. HD-DOT has been very successful at mapping distributed brain function and networks [Eggebrecht2014] throughout the whole human brain with mm location errors [Wu2014]. The method relies on a high-density array of sources and detectors and either prior known subject specific models (obtained using, for example, MRI), or a human brain atlas to form images with high spatial resolution.

The spatial resolution limits of DOT can be understood in terms of diffuse photon density waves (DPDW), which are wave solutions to the diffusion equation given in (10). In the frequency domain, and assuming the light is modulated with an angular frequency ω, the average intensity within a turbid medium obeys the Helmholtz equation with wave number $k_o = (-\mu_a/D + i\omega n/cD)^{1/2}$, where i is the square root of negative one. Note that the wave number is always complex (even when there is no absorption) because of loss by diffusion, giving $k_o = k_r + ik_i$. The amount of spatial information propagated through the highly scattering medium by a superposition of DPDW limits the spatial resolution of the imaging method [Rip1999]. In free space, propagating scalar waves give rise to the well-known Rayleigh resolution limit of $\lambda/2$ due to the exponential decay of near field or evanescent waves. Interestingly, DPDW are typically measured in the near-field due to their long wavelength ($\lambda_o = 2\pi/\mathrm{k_r}$ being 7.53 cm in breast tissue) meaning all wave solutions propagate to the detector. Therefore, assuming sufficient source-detector diversity, the resolution of DOT is fundamentally limited only by the SNR at the detectors. However, if we consider the superposition of DPDW, the propagation transfer function (details in [Rip1999]) is given by $F(\boldsymbol{K}, z) = \exp[iq(\boldsymbol{K})z]$, where $|\boldsymbol{K}|^2 + q^2 = k_o^2$, implying $\boldsymbol{K} =$

(K_x, K_y) is a real vector, and $q(\boldsymbol{K}) = (k_o^2 - |\boldsymbol{K}|^2)$. Since $q(\boldsymbol{K})$ is always complex due to loss by diffusion, the amplitude and phase of the DPDWs decay exponentially with distance, effectively making $F(\boldsymbol{K}, z)$ a spatial frequency filter which dampens high spatial information below the noise floor of the detector. This dampening causes the spatial resolution to decrease exponentially with depth (z). With current detector technology, resolutions between about 1 mm [Gra2003] and 1 cm (depending on depth) are typical for DOT. Graves et al. achieved 0.7 mm resolution through 0.75 cm (with the assistance of fluorescence) giving a resolution of about depth/10. As optical detector technology and ODT algorithms continue to progress however, better spatial resolutions should become possible.

2.7. Current Technology

We present some critical aspects of the relevant instruments in this section. An important parameter is the required speed of measurement, dictated by the velocity distribution of the scatters, in relation to concomitant requirements on the sources and detectors.

2.7.1. Spatial Optical Modulators

There are several sub-classes of spatial phase modulators that are relevant. Deformable mirrors are used broadly in adaptive optics applications. They tend to have a small number of active elements (~100 - 1000) and are generally deemed to be less useful for speckle-field type wavefront engineering. Liquid crystal-based SLMs are extensively used in wavefront control research. SLMs are currently available with pixel counts up in the range of megapixels and response time of 1-10 ms. Liquid crystal-based methods are intrinsically limited in their response time - 1 ms is likely the practical limit for this technological approach. Digital micromirror devices (DMDs) are another means for wavefront shaping that is limited to binary phase or amplitude modulation. The benefit of this approach is that the technology is semiconductor based and directly scalable for higher pixel count, and it has the potential for high-speed operation. Having a larger pixel count is generally more desirable than a higher number of levels in phase control.

2.7.2. Cameras

Not all wavefront methods discussed require optical wavefront detection. For those that do, high speed and high pixel count are the two primary considerations. Achieving a sensitivity near to the shot noise limit is generally not considered a particular challenge as the wavefront measurement process generally involves the use of interferometry, and shot noise level detection can be accomplished as long as the reference field is sufficiently strong (because the reference arm provides gain). The pixel count is currently in the 10-100 megapixel range. The bit depth of the camera is relevant in most applications. During interferometry measurements, the signal is weak and riding on top of a strong DC background (due to the strong reference field). A large bit depth camera ensures that we are able to detect that weak signal. A 16 bit camera is generally used, but it is the last 2-4 bits in the measurements that are critical. The high bit count has the unfortunate downside of creating a high data volume download burden from the camera. A camera that is capable of only measuring the weak relevant signal (which can be made to oscillate) is highly desirable for this research area.

In DOT, a gated image intensifier can be used on a camera. Application of a gate signal allows the temporal response of the modulated light detected to be determined as a function of position, as imaged onto each pixel in the camera. This type of technology can potentially be applied to address the weak signal on a large DC problem stated previously. One challenge for in vivo experiments is the read-out time for such cameras.

3. Research Opportunities

3.1. Practical Limits on Amount of Scatter

3.1.1. Stationary, Spherical Cloud Model

Consider a coherent source that continuously emits power *P*, surrounded by a uniform, perfectly transparent scattering medium (say a laser inside a cloud). Imagine a spherical cloud of radius *R* with the source at the center. Since there is no absorption, clearly the power leaving the cloud at steady state is *P*, which is uniformly distributed over the surface. Assuming a speckle spot radius of λ/2, the power per speckle at distance *R* is $P_s(R) = P\lambda^2/16R^2$. Take a *P=10*W laser or 10^{20} photons/s (most lasers are of that order), to do any useful wavefront control, we need to detect some minimum power above detection noise, say 1 photon/s per speckle, so must have $R<10^9\ \lambda$ or *R*~1 km. A more realistic requirement of 10^4 photons/s per speckle will reduce the distance to ~100m.

3.1.2. Requirements on Coherence

We consider the source coherence requirements, for the spherical cloud picture under the assumption that the medium is perfectly stationary. The centrally located light reaches the surface at radius *R* after reverberating through the medium. The shortest path is *R*, but the average distance travelled by a photon is R^2/l^*, which is also approximately the spread in arrival times. In order to obtain a stable speckle pattern with high visibility, the coherence length has to be of that order. Taking *R*=1 km, and l^* =10 m, (i.e., assuming 100 scattering lengths) will require a coherence length of 100 km, that is, the spectral width of the laser must be below ~10 kHz, and the result is 100kHz for *R*=100m. This is not your everyday laser. Note also that if the goal is to establish a communication link between the source and the detector, the information (modulation) rate needs to be lower than these rates to preserve coherence.

The diffusion model provides valuable information about the coherence requirements for a laser to penetrate a scattering medium and produce speckle [Mck2000]. Monochromatic light forms speckle with the contrast ration of unity regardless of the amount of scatter, but even very coherent laser sources may have coherence lengths on the order of hundreds of meters. Control of coherence can be used as a basis for imaging [Mck2000]. More relevant in appraising the degree of scatter that can be accessed is the source coherence requirement from the diffusion model. The normalized *p(t)* is the travel time distribution, and transformation to length gives the path length density function, *p(l)*. The width of *p(t)*, say measured by σ_t, indicates a measure of the laser coherence, so the bandwidth of the light source should satisfy BW $< \cdot 1/\sigma_t$. Clearly, coherent communication through increasing scatter requires an increasingly coherent source.

3.1.3. Absorption

The estimations in Sections 3.1.1 and 3.1.2 assume that the medium is perfectly transparent. However, even weak absorption can be significant because the light effectively travels a much longer distance than the physical distance. Light at 1 micron loses about 50% in 3 km to water vapor absorption in air (probably much more inside a cloud); hence, there will be practically no light emerging from a 1 km cloud at this wavelength. At 100 m (and ~10 km effective travel per photon), the transmission would be ~10%. However, we note that the absorption loss is much less drastic for light at 400nm – absorption is 3 orders of magnitude lower. The transmission would be commensurately improved at the shorter wavelength. This exercise emphasizes the need to tailor the wavelength to the vicinity of 400 nm if absorption is expected to have a large negative impact. The interplay between scattering, absorption and wavelength choice is an interesting one. We can see here that a shorter optical wavelength is favored for absorption considerations, while a longer wavelength is desired for minimizing scattering. The exact

choice of wavelength is dependent on the scenario in consideration. For example, in aerial surveillance, a shorter wavelength is likely desirable to minimize the substantial absorption associated with the long distances. For medical applications, longer wavelengths to minimize scattering is likely more desirable.

3.1.4. Dynamics

To perform coherent wavefront shaping in a dynamic medium, the measurement system has to be faster than the fluctuating speckles. If the speckle pattern is changing at a kHz rate, a satisfactory number of photons must be measured in 1 ms, and really much faster in order to use the information to control the system before the pattern changes. This will reduce the above maximal distances to ~100 m (to detect just one photon, and ~10 m allowing a larger dynamic range).

3.1.5. Detector Noise

Detector shot noise (due to randomness in the arrival of photons or the generation of charge in the detector) and thermal noise (due to the physical temperature of the detector, or in the equivalent sense, due to the environment noise at the detector, along with the signal) limits all communication and imaging systems. The detector noise therefore dictates source energy, for an active system, and integration time or detector bandwidth. In turn, the detector speed dictates the possible dynamic media. The SNR can be calculated as μ_i^2/σ_i^2, where μ_i and σ_i^2 are the photocurrent mean and variance induced at the detector by the incident photons. The mean and variance can be approximated as $\mu_i = eJ\eta$ and $\sigma_I^2 = 2e\mu_i B + (4k_B TB)/R$ for shot and thermal noise, respectively, where e is the charge of an electron, η is the detector quantum efficiency, J is the photon current or power detected, B is the detector bandwidth, k_B is Boltzmann's constant, T is temperature, and R is the effective static resistance of the detector. Here, the $2e\mu_i B$ term in the variance reperesents shot noise, and the $(4\kappa_B TB)/R$ term gives the thermal noise. This simple picture provides a design budget for communication in randomly scattering media.

3.1.6. Scaling of Scatter

To obtain the scattering mean free path, $\ell_s = 1/(\rho\sigma_s)$, we need the scattering cross section of a single scatterer, σ_s, and the density of scatterers, ρ. For water droplets, the scattering cross section has been shown to be comparable to the geometrical cross section over a wide range of radii [Hou1949]. Assuming that the radius of water droplets is 1 μm and using a relatively low density of 10^9 m^{-3}, the scattering mean free path is found to be 1 km. A diffusion model would hold for scattering medium thicknesses more then several km. The parameters describing the scattering medium can be scaled by α (on the order of 10^5 for scaling laboratory distance to large distance, or 10^{-5} for scaling the large distance to laboratory distance), resulting in $\tilde{r} = \alpha r$, $\tilde{c} = \alpha c$, $\tilde{\mu}_a = \mu_a/\alpha$, $\tilde{\mu}_s = \mu_s/\alpha$, and $\tilde{g} = g$. Note that the distances between scattering and absorption events (l_s and l_a) are scaled by a factor of α. This scaling allows a material with widely-spaced scatterers to be modeled by a more densely packed material (in the lab). The scaling of the velocity requires the scaling of the refractive index, however, the velocity is not needed in the case of unmodulated light ($\omega = 0$). Additionally, in the case where there is no or little absorption, the scaling can be written as $\tilde{g} = g$, $\tilde{\mu}_s = \mu_s/(\alpha)^2$, and $\tilde{c} = c$, where the scaling of the velocity is absorbed by the scattering coefficient. Without velocity scaling and with absorption, both the time and transmittance are scaled by a factor of α. In this case if we integrate over time to find energy, we find that in the condensed medium the output energy is increased by a factor of $1/\alpha = 10^5$, meaning the detected power through a condensed medium can be directly related to the detected power through a cloud, even without velocity scaling.

3.2. Source and Detector Configurations – Space, Time, and Frequency

3.2.1. Spatial Extent and Degrees of Freedom

With coherent light, whereby speckle occurs, the phase and amplitude of incident light can be controlled as a function of position (or equivalent signal processing applied, yielding spatial diversity or MIMO, and perhaps incorporating spectral diversity), there are opportunities to extend the penetration depth beyond that suggested by a statistical average picture. If the medium can be considered stationary for a suitably long period for the field Green's function, of the governing partial differential equation for the light fields, or the transmission matrix or scattering matrix for modes, to be determined as a function of frequency, then focusing light through arbitrary scatter is in principle possible, provided absorptive loss is negligible. The efficacy would then be limited by the spatial support of the optical control, by the degrees of freedom (pixilation), and by other practical issues such as the need to control light with lenses and mirrors. While overall scattering loss may increase with degree of scatter, reducing the energy in the focus (because of backscattering), with certain arrangements and separate control, special matching may be possible that would ideally allow most of the 'signal' to be coupled to the focus. The primary limitation is then the required measurement speed, dictated by the velocity (distribution) of the scatters, and of course the detector SNR, again with performance dictated by the technology. By exploiting information related to (natural) motion of a source or object, requirements to characterize the scattering medium could be relaxed and the communication or imaging problem simplified. Information measures may provide guidance on necessary data and ways to quickly process or interpret scene or sensory data.

3.2.2. Control of Energy Transport Through Scattering Media

While control of the fields (sources) over a closed boundary coupled with knowledge of the Green's function for the scattering domain precisely specifies the fields at all points inside or outside the closed boundary, the ability to couple energy used to set up those sources is a separate question. Furthermore, while necklace states that exist in strongly scattering media that exhibit Anderson localization provide energy transport channels, it seems unlikely that these will be significant in the more weakly scattering (with heavy overall scatter) media that are most common in nature.

Consider M propagating modes in a waveguide that has a region containing random scatterers. Control of the M incident mode complex coefficients could control the mode coefficients on the transmission side. Separate would be the question of reducing the reflection coefficient for all incident modes to zero, i.e., of coupling all of the incident energy through the random medium. This would require more degrees of freedom in the incident field. This could occur by having two different waveguides or otherwise allowing control of M incident modes to influence N modes at the region on interest, where $M > N$. We can extend this idea to scattering media in unbounded space, where M pixels or spatial modes are used to control N basis functions (modes, for instance) at the object/receiver/position of interest. The control of energy delivered to the region of interest is proportional to $(M+N)/N \approx M/N$ *for* $M >> N$.

Energy delivery can therefore be impacted by wavefront control. The number of control elements in relation to the degrees of freedom at the region of interest dictates the fraction of the incident energy that can be delivered. For discussion of this picture, refer to Sections 2.3 and 2.4.2.

3.2.3. Source and Detector Arrangements – Spatial Diversity

One of the important applications of wavefront shaping lies in imaging through biological tissue. Moving an ultrasound focus, for instance, allows light intensity at different position within the tissue to be sampled. The memory effect [Fre88] is also utilized to shift the optical focus behind the scattering medium [Kat2014b]. However, such scanning methods require a guide star and are typically slow. To

overcome such problems, a convolution between the fluorescent object and the speckle field that excited the fluorophore, shifted using the memory effect, was employed [Ber2012]. A Gerchberg–Saxton-type iterative algorithm was then applied to reconstruct the object behind the scattering layer. This imaging technique was soon applied to image blood cells beneath chicken skin [Yan14]. Instead of shifting the excitation field, Katz *et al.* [Kat2014b] calculated the autocorrelation of the object with just a single shot of the camera. The researchers successfully reconstructed the image of the objects behind a 0.5 mm thick chicken tissue using the same phase retrieval algorithm. Interestingly, Katz's method does not need to actively shape the wavefront; instead, the object itself shifts the speckle (point spread function) on the camera plane.

Correlations over source position with distance steps large relative to the wavelength provide information about the fields incident on a randomly scattering medium, in principle regardless of the degree of scatter [New2012, New2014b] and distinct from the memory effect [Fen1988, Ber1989]]. Figure 9 shows recent efforts from the Webb group that allowed the field incident through two apertures to be determined from speckle images on the other side of a heavily scattering medium. This result will open avenues for communication, imaging, and control through heavily scattering media and may facilitate determination of the transmission matrix or Green's function.

We outline the mathematical basis. Consider a Green's function representation to describe the (polarization-dependent) speckle field correlation [Wan2010, New2012],

$$\langle \tilde{\boldsymbol{E}}[\boldsymbol{U}(\boldsymbol{r})]\tilde{\boldsymbol{E}}^{*}[\boldsymbol{U}(\boldsymbol{r}+\boldsymbol{\Delta r})]\rangle = \int_{\boldsymbol{r}'} \boldsymbol{U}(\boldsymbol{r}';\boldsymbol{r})\boldsymbol{U}^{*}(\boldsymbol{r}'+\Delta\boldsymbol{r};\boldsymbol{r})\langle|\boldsymbol{G}(\boldsymbol{r}_{\boldsymbol{d}},\boldsymbol{r}')|^{2}\rangle \boldsymbol{d}^{\boldsymbol{2}}\boldsymbol{r}', \tag{18}$$

where $\boldsymbol{r}_d$ is the detector position, $\boldsymbol{r}$ is the object (source) position, $\Delta\boldsymbol{r}$ is the translation vector, *U is the field incident on the scattering medium*, *E* is the field scattered from the random medium at the detector, and *G* is the field Green's function that is averaged over scatterer configurations. In the limit of sufficient scatter, the Green's function term is reduced to a constant and the correlation can be rewritten using a plane wave superposition as

$$\langle \tilde{I}[U(\boldsymbol{r})]\tilde{I}[U(\boldsymbol{r}+\Delta\boldsymbol{r})]\rangle \approx \left|\mathcal{F}^{-1}\{\left|U_k(\boldsymbol{k}_{\parallel})\right|^{2}\}\right|^{2}, \tag{19}$$

where $\mathcal{F}$ represents the Fourier transform. Remarkably, the *field incident on a scattering medium can be reconstructed by measuring the resulting intensity speckle images* (Figure 9(b)).

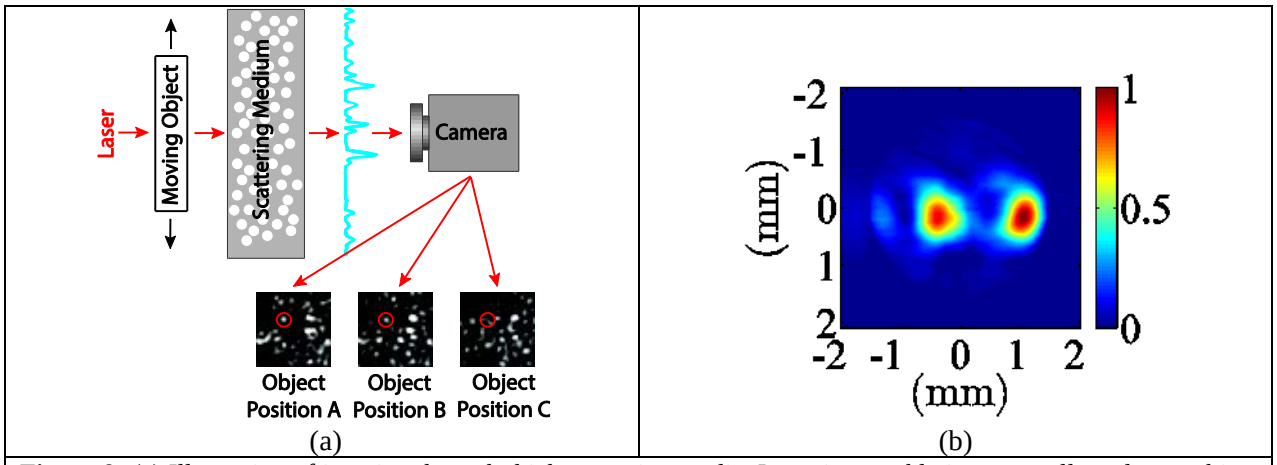

Figure 9: (a) Illustration of imaging through thick scattering media. Intensity speckle images, collected over object position, are used to reconstruct the field from a laser-illuminated object that is incident on a randomly scattering medium. The red circle in the speckle images shows how the speckle image evolves as the object moves. (b) Reconstruction using our speckle imaging method showing the magnitude of the field shaped by a two-hole aperture. The shaped laser beam was incident on a 9~mm thick slab with $\boldsymbol{\mu}'_{\boldsymbol{s}}$ = 4 cm^{-1}. For details, see [New2014b].

3.3. Decorrelation Time and Scatterer Velocity Density Functions

3.3.1. Physical Media

Physical scattering systems move, and this motion presents challenges for optical instruments. Examples are aerosols, turbid water, and biological tissue. The velocity distribution of the scatterers becomes an important measure that will drive certain technologies and pose limits on approaches. Using an optical measure, the decorrelation time of speckle patterns provide characteristic information about the dynamic scattering medium and also a metric for detector integration time. In addition, the sources and detectors may be moving. While substantial use of the decorrelation of speckle patterns has been used in biological applications, diffuse wave spectroscopy (DWS) for instance [Pin1988], there is a dearth of data related to various dynamic media that could be of interest. Such media may have velocity density functions that are quite complex, with various regions having different characteristics – associated with vortices, for instance. We suggest efforts to characterize dynamic media would produce useful data for coherent communication and control work, which would also drive measurement time scales and the associated technology requirements.

Using wavelengths within atmospheric windows, communication signals propagating through the air are subject to the attenuation due to the absorption and scattering by natural or anthropogenic aerosols [Col2007, Hin2012]. To model scattering environment relevant to application, the dynamic scattering by various types of aerosols (sulphate, dust, rain, fog, and cloud) under different situations (e.g., wind speed, temperature, humidity) must be studied in detail. Substantial work has been done to characterize the aerosol optical properties in relation to the aforementioned factors [Wel1977, Hop1990, Dow1993, Mel1994, Hess1998, Mel2001], and to remotely sense the optical properties of static aerosols over oceans [Tan1997]. *In vivo* tissues are highly dynamic and relevant time constants have been used in imaging with speckle [Boa1995]. Despite these efforts, progress in any particular application will rely on data specific to that situation.

Can a subset of the scatterers be involved in communication that are moving more slowly? If so, this could facilitate coherent imaging.

3.3.2. Simple Models

In an ideal gas, the particles' velocity is well described by the Maxwell-Boltzmann velocity distribution [Rei965], which gives the statistical velocity distribution of freely moving particles undergoing elastic collisions at or near thermodynamic equilibrium, resulting in the density function [Hin2012]

$$f(v) = \sqrt{(\frac{m}{2\pi kT})^3}\, 4\pi v^2 \exp\,(-\frac{mv^2}{2kT}), \tag{20}$$

where v is the velocity of a particle, m is the particle mass, k is Boltzmann's constant (1.38×10^{-23} J/K), and T is the temperature in Kelvin. The mean velocity is [Hin2012]

$$\langle v\rangle = \sqrt{\frac{8kT}{\pi m}}. \tag{21}$$

If we assume an average particle mass of 6.5×10^{-14} kg, corresponding to micrometer sized particles, and a temperature of 273 K, the mean velocity is 3.4×10^{-4} J/K m/s. This gives around 2.9 ms before the particles, on average, have moved about a wavelength (1 μm). Within this time interval, speckle images can be collected and the primary contributions to the spatial correlation can be attributed to the movement of an embedded object.

In another model, aerosol particles can be described by a Reynolds number, the ratio of inertial to frictional forces, a number less than 1. This region is referred to as the Stokes region, where Stokes' law states that the drag force on a particle can be described as [Hin2012]

$$F_D = \frac{\pi \rho_g d_p^2 v_p^2 C_D}{8}, \tag{22}$$

where $C_D$is the drag coefficient, ρ_g is the density the gas and v_p is the relative particle velocity. When a particle is released in air, it quickly reaches its terminal settling velocity, where its drag force equals to the gravitational force, [Hin2012]

$$v_{TS} = \frac{\rho_P d_P^2 g}{18\eta}, \tag{23}$$

where ρ_P is the density of particles, d_P is the diameter of the particle, g is the gravitational field strength and η is the dynamic viscosity coefficient. In a microscopic picture, water droplets are constantly falling at different terminal speeds according to their mass. In warm clouds formed of water droplets, larger droplets fall at a higher terminal velocity due to their larger drag force. The large droplets will coalesce with smaller droplets to form even larger ones, triggering precipitation. Water droplets can be categorized into small cloud droplets (1 μm to 20 μm in diameter), large cloud droplets/small raindrops (20 μm to 1 mm) and large raindrops [Bea1976]. It has been shown that terminal velocities of droplets having various sizes can be modeled. For a cloud droplet with diameter of 20 μm, the terminal velocity would be around 0.1 m/s [Bes1950]. To test this, estimation can be made based on (19). Assuming standard air pressure and temperature at 273 K, the same diameter (20 μm), the terminal velocity calculated is 0.0119 m/s, which agrees with a more sophisticated model [Bes1950]. In such situations, the faster motion and shorter speckle measurement time window is still feasible.

3.3.3. Correlation Time Metric

The temporal resemblance in speckle intensity pattern, commonly referred as speckle autocorrelation function, is used as a conventional measure of scatterer movement. Mathematically, the correlation between the speckle patterns at time t_0 and $t_0 + \tau$ can be defined as [Dur2010]

$$g_2(\tau) \equiv \frac{\langle I(t_0) I(t_0+\tau) \rangle}{\langle I \rangle^2} - 1, \tag{24}$$

where $I(t)$ is speckle intensity at time t and the brackets ⟨ ⟩ denote the ensemble average. The autocorrelation function gradually decays from 1 to 0 as the scatterer movement constantly changes the resultant speckle pattern.

The temporal fluctuation of the scattered light field provides useful information about the dynamics of a given sample (e.g., the velocity distribution and direction of the scatterers). For instance, when the light is scattered by a particle subject to Brownian random motion, $g_2(\tau)$ exponentially decays with the time constant $1/2Dq^2$, where D is the particle diffusion coefficient and q is a scattering wave vector magnitude. For the case of directional flow, $g_2(\tau)$ equals $e^{-q^2 v^2 \tau^2}$, where v is the velocity of flow [Dur2010].

When the light is multiply scattered, as in tissue, $g_2(\tau)$ varies with scattering path length. For the case of non-interacting Brownian scatterers, $g_2(\tau)$ [Mar1987] is given by

$$g_2(\tau) = e^{-(\tau/\tau_0)(s/l^*)}. \tag{25}$$

The quantity τ_0 is a single scattering relaxation time defined by $1/D(2k_0)$, where k_0 is the free space wave number, D is the diffusion coefficient, and l^* is the TMFP. With multiple scattering, $g_2(\tau)$ also follows an exponential decay model but the decay time constant is inversely proportional to the scattering path length. More details on the relevant theory are in the literature [Ber2000, Dur2010].

The technique, by which useful information can be inferred from the speckle autocorrelation in the multiple scattering regime, is called diffusing wave spectroscopy (DWS) [Pin1988, Mac1989, Dur2010]. Many interesting aspects of tissue dynamics have been discovered by the use of DWS.

First, the motion of blood cells mainly contributes to the fast decay of $g_2(\tau)$. Though cells and their organelles are moving in a fluidic environment of tissue, the extracellular matrix (e.g., collagens, elastic fibers, proteoglycans) mechanically support the cells so that the movement is very slow compared to the motion of blood cells. For instance, the speed of red blood cells in rat arteriole is 1~3 mm/sec and

the cell migration speed of a human cancer cell and T-lymphocytes in collagen matrix is around 0.1~0.3 and 7~10 um/min, respectively. T-lymphocytes are known as highly motile cells as it use a cell-adhesion receptor for its migration towards foreign antigen while the cancer cells destructively migrate through the extracellular matrix.

Second, $g_2(\tau)$ fits well with the Brownian model of scatterer movement over a wide range tissue types, such as rat brain and human muscle. This is a reasonable result considering that the motion of blood cell is not ballistic inside the microvasculature (e.g., capillaries, arterioles, and venules). Though the blood flow in the main arteries and veins is ballistic, light is mostly absorbed when it propagates through the main blood vessels.

Third, the $g_2(\tau)$ decay time constant has a range from several microseconds to several seconds, depending on the collection geometry, sample thickness, blood cell concentration and pressure applied on the tissue. Because the collection geometry and sample thickness determine the distribution of path length of diffused photons, it is clear from (25) that the two parameters significantly affect the decay time. Blood cell concentration plays an important role in determination of the effective l^* in (25). When tissues are immobilized with some pressure, the motion of blood cell is restricted. In turn, $g_2(\tau)$ decays slowly. One example presenting fast dynamics is brain tissue. In the case that speckle fluctuations from the adult human brain is measured in a backscattering geometry, the decay time is on the order of tens of microseconds [Dur2004]. In contrast, a tightly clamped rabbit ear presents a decay time of a few seconds [Cui2010a].

Our ability to perform wavefront shaping depends on the medium being stable during the process, or more specifically the stability of the transmission matrix. The transmission matrix stability can be directly quantified through its transmitted speckle correlation. Ref. [Jan2015] details the derivation. Succinctly put, the efficiency of our wavefront shaping ability can be directly quantified as

$$\frac{PBR(t_0+\tau)}{PBR(t_0)} = g_2(\tau)$$

$$= \frac{\langle I(\tau)I(t_0+\tau)\rangle}{\langle I(t_0)\rangle^2} - 1, \tag{26}$$

where $g_2(\tau)$ is the correlation function of the speckle intensity at time t and $t_0+\tau$. Equation (26) is useful as it means that we can predict the performance of wavefront shaping once we determine the speckle decorrelation characteristics.

Now that we have connected the wavefront shaping efficiency to the speckle decorrelation, we can make use of a number of established works to predict how the wavefront shaping efficiency is going to be impacted by random medium thickness and other medium characteristics. Based on the work of Pine *et al.* [Pin88] and Maret and Wolf [Mar87], the speckle field correlation $g_1(\tau)$ is given by

$$g_1(\tau) = \langle E(t_0)E(t_0+\tau)^*\rangle \propto \int_0^\infty P(s)\exp\left[-(2\tau/\tau_0)(s/l')\right]ds, \tag{27}$$

where s is the optical path length within the scattering medium, l^* is the transport mean free path, τ_0 is the characteristic diffuse time of the scattering medium, and $P(s)$ is the probability density function of the scattering path length. This equation shows that $g_1(\tau)$ decays by $\exp\left[-\left(\frac{2\tau}{\tau_0}\right)\right]$ per scattering step. The first order correlation $g_1(\tau)$ and second order correlation $g_2(\tau)$ can be bridged using the Siegert relation,

$$g_2(\tau) = \beta|g_1(\tau)|^2. \tag{28}$$

This set of relationships allows us to make some direct experimentally based predictions. In Ref. [Jan2015], the speckle decorrelation time is experimentally found to be ~2.5 seconds for live tissue of thickness 1.5 mm at a wavelength of 532 nm. Because the decorrelation time decreases with the square of the thickness, this implies that a wavefront shaping system with a response time of 10 ms will be able to usefully work with live tissue of 24 mm thickness. For a system with a response time of 1 ms, this thickness limit increases to 75 mm. For a measurement system with infinitely fast response, the light transport time imposes a thickness limit of 30 m.

3.4. Information Measures

How many measurements are needed to construct a digital image? Naively, one expects a number of measurements equal to the number of pixels (N^2 in an $N \times N$ – pixel image), and this is exactly what the *sampling theorem* from signal analysis predicts [McK2004]. However, most images have a mathematical property known as "sparsity", whereby it is possible to transform the image data to a representation that uses less memory [Cov2006]. An example of a representation in which most images are sparse is the wavelet basis [Dau1992]. This property is widely used to compress pictures and movies on the Internet, e.g., in the jpeg2000 format, and is even included in many cameras so that most of the measured image data are discarded even before storing. With regard to light in randomly scattering media, mutual information [Cov2006] addresses the question of the additional information provided by, for example, spatial or spectral diversity.

Compressive sensing (for reviews see, e.g., [Can2008, Dav2012]) introduces compression already in the measurement process [Can2006, Don2006, Dua2008]. Much of the data that would be discarded in compression is never even measured, leading to a speed-up that is especially important in scanning imaging methods where a single detector is used instead of an array. In compressive sensing, the intensities of combinations or groups of image points are measured instead of single image points, as illustrated in Figure 10. Surprisingly, this works very well especially if the sensing configurations are pseudo-random and not related to the image. Data processing is then used to synthesize an image from the measurements. As important examples, metamaterials can produce sub-wavelength sampling patterns [Hun2013] and even random speckle is an excellent basis for compressive imaging [Kat2009, Car2009, Liu2014, Jan2014, Taj2014].

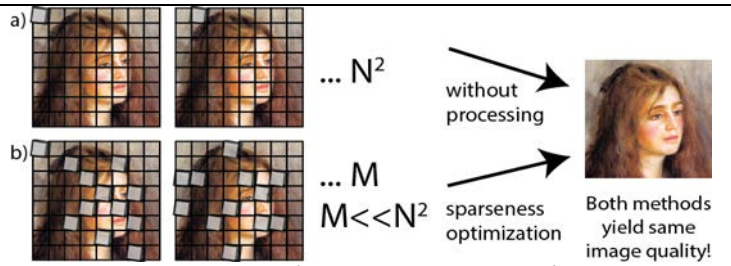

Figure 10: Cartoon of compressive imaging: (a) In conventional imaging one probes an image pixel-by-pixel to construct a digital representation. The number of probes is $\mathbf{N^2}$ for an $\mathbf{N \times N}$ –pixel image. (b) In compressive imaging one probes the average intensity of collections of pixels. An algorithm optimizes sparseness to obtain an image of equal quality from a much smaller number of measurements.

3.5. 'Bootstrap' Imaging Methods

It has been shown in recent experiments to be possible to image at high resolution and contrast through media with a known transmission matrix. Current methods for transmission matrix measurements are invasive and are not useful if access to the object side of the medium is unavailable. However, if the transmission matrix of a thin slab of scattering medium can be inferred form backscattered light, it may be

possible for an imaging apparatus to perform a "bootstrap" procedure where one first images the first layer (of order one mean free path in thickness), and determines its structure. From the structure, by solving the wave equation, it is possible in principle to obtain the transmission matrix of such a layer. This involves rather heavy calculations, as present finite-difference or finite-element methods need large amounts of computer memory and processor time. Then, using the transmission matrix of the first layer, it should be possible to perform the same procedure on the second layer, and so on *ad infinitum*.

For the purpose of this document, we assume infinite computing power is available, but in practice this assumes enormous advances in software engineering and computing hardware. Here, we estimate in which cases optical measurements will give the algorithms even in principle enough information to start such computations in a meaningful way.

The information content of the medium can be estimated using a simplified model [Skoric2008]. In dense scattering media such as tissue, a minimum amount of information is knowledge of the index on a grid with point spacing of at maximum $\lambda/2$. Approximating the medium as a binary mixture, at least one bit per grid point is needed, leading to an information density (entropy) of 8 bits per cubic wavelength, or about $\rho = 10^{10}$ bits/mm^3. As a result, a channel of width 1 mm^2 and depth L will contain an amount of information of 10^{10} (L/mm) bits.

A laser of power 1 W will emit about 10^{19} photons per second. The photons will spread sideways into a cone. Up to a depth L, this cone has a volume of order L^3, and an entropy of about 10^{10} (L/mm)^3 bits. Assuming we need of order 1 photon per bit, and 1 in 10 photons is usefully backscattered, we need to detect 10^{11} (L/mm)^3 photons. In 1 s period the maximum achievable L is therefore about 400 mm, and in 1 ms the maximum depth is 40 mm. These estimates are based on information content and apply to all dense media. These are information theory based maximum ranges. Realistic bounds might be an order of magnitude lower.

In conclusion, in tissue-like media bootstrap methods may provide useful imaging and the possibility of wavelength-resolution focusing up to a depth of 40 mm. This would enable sub-cellular resolution imaging of almost all human organs.

Sparse media such as aerosols or atmospheric conditions consist of droplets or particles in air. To microscopically describe scattering in such media, one does not need a high-resolution grid. Instead, the positions and sizes of all particles in the volume of interest should be known. Let us assume a dense fog has a density of 1 particle per mm^3 [She2010b], then the volume information density is of order 100 bits/mm^3. Assuming the same 10% efficiency of back scattering, the number of photons needed is 10^3 (L/mm)^3. In 1 second the maximum L is 21 m, in 1 ms it will be of order 2.1 m. Since this is smaller than the mean free path in most fog conditions, it is to be concluded that the use of bootstrap-style methods in aerosols or fog will be more challenging.

Sandstorm conditions contain particles at a density much lower than 1 particle per cubic mm. For dense sandstorms (particle size in the 20 μm range) we find a similar result: At a visibility in the range of a few m there will be 1 particle per mm^3 and the same reasoning applies.

For turbid water the situation depends on the density of particles. Rain and snow, with a much lower number density or much larger particles may be more amenable to bootstrap imaging. Layered media such as plant and tree foliage or cloth are likely to be quite amenable to bootstrap imaging as the scatterers are sparsely distributed in space, however more analysis is needed for the specific case.

An interesting speculative improvement is worth considering: What if it was possible to confine the probing light in a narrow beam? Such a beam would need to be confined by knowledge of the scatterer positions, hence would be confined by scattering to a radius of necessarily about 1 transport mean free path l^*. The amount of information in the beam is $\pi \ell^2 L \rho$. For a medium with information density ρ, incident photon flux Φ and measurement time τ, we find the maximum depth that can be reached is

$$L_{max} = \frac{\Phi \tau}{\pi \ell^2 \rho}. \tag{29}$$

Counter-intuitively, the depth range decreases with the mean free path now! In a fog with $\ell = 10$ m the maximum range for this type of method (with a 1 ms correlation time) now is 500 m, which is a substantial improvement. However, no path toward implementation of this method currently exists.

3.6. Critical Factors in Wavefront Control Speed

What is possible with regard to the ultimate scatter limit is fundamentally dictated by detector noise. The practical limits of scatter that can be penetrated are based on the technology, with better sources and detectors and certain schemes developed with specific technology (such as what we have today) allowing greater penetration of scatter. Consider the anecdotal application in a car where the headlights are reflecting from fog without significant penetration. Imagine headlights achieved with RGB lasers that electronically scan the road ahead and compensate the spatial distribution of the light using conformable large area control elements that employ aspects of technology currently being developed. In this way, the headlights compensate so that the driver can see the road ahead. While seemingly a challenge today, such a concept is plausible.

3.7. Guidestar Analysis

This analysis is aimed at illustrating some of the constraints involved in guidestar-based phase conjugation focusing of light within a scattering medium. For simplicity, we assume the target sample to be a turbid sphere (spherical cloud) for which we would like to focus light at the sphere's center.

As a process, one would first flood the sphere with light. A guidestar would then be activated to tag the light traversing the sphere's center. The tagged light wavefront would then be detected at the sphere's surface. The total exposure and collection time would be τ. A phase conjugate light field can then illuminate the sample and form a focus at the sphere's center. We assume that the sphere is sufficiently turbid that speckles are fully developed and the diffusion approximation holds. We further assume that the absorption coefficent is negligible. The overriding limiting constraint here is the amount of tagged light we can harvest in the recording process. To be able to generate a adequate wavefront for playback, we require the detection of M tagged photons on the detection side. M is a fixed practical quantity and $M = 10^5$ is a good benchmark quantity for practical considerations. This gives us

$$M = \frac{E_s I_{target} A \tau}{hf\ 4\pi r^2} N \left(\frac{\lambda}{2}\right)^2 \tag{30}$$

where E_s is the guidestar efficiency (the fraction of photons tagged during interaction), I_{target} is the irradiance at the target location, A is the guidestar interaction cross-section, τ is the interaction time, $\left(\frac{\lambda}{2}\right)$ is the speckle spot size, hf is the energy quantum of the photons involved, r is the sample radius (or the penetration depth), and N is the number of controllable optical modes. τ is limited by the sample speckle decorrelation time because we need to perform the collection process in a time shorter than the decorrelation time. For a fully diffusive medium, the decorrelation time is inversely proportional to the square of the sample's lateral dimension (or r). Taking this into consideration, we can rewrite (30) as

$$M = \frac{E_s I_{target} A \alpha}{hf\ 4\pi r^4} N \left(\frac{\lambda}{2}\right)^2 \tag{31}$$

where α is the decorrelation time coefficient.

As a point of reference, living tissues with pulsating blood flow has a decorrelation time that is ~ 30 ms for 2 mm thick tissue, which implies $\alpha = 1.2 \times 10^{-7}$ m^{2}s. I_{target} is limited by tissue damage threshold consideration and is nominally set at 100 mW/cm^2. N ultrasound guidestar has an efficiency of ~ 0.01. By

substituting these realistic practical numbers into (31), we arrive at a relatively simple order-of-magnitude relationship for tissue depth penetration (equals r) in the context of guide-star based focusing as

$$r \sim 1 \text{ mm} \, . N^{1/4} \tag{32}$$

This equation is interesting in that it highlights the fact that one needs a 4 orders of magnitude increase in controllable optical modes to yield an order of magnitude increase in depth penetration.

3.8. Technology

Faster and more sensitive detectors will provide for an increase in the amount of scatter. There are opportunities with improved single and array detectors - the noise (notably thermal, to approach the shot noise limit), read-out time for CCD cameras (which limit their speed), data transfer time from detectors to spatial light modulators.

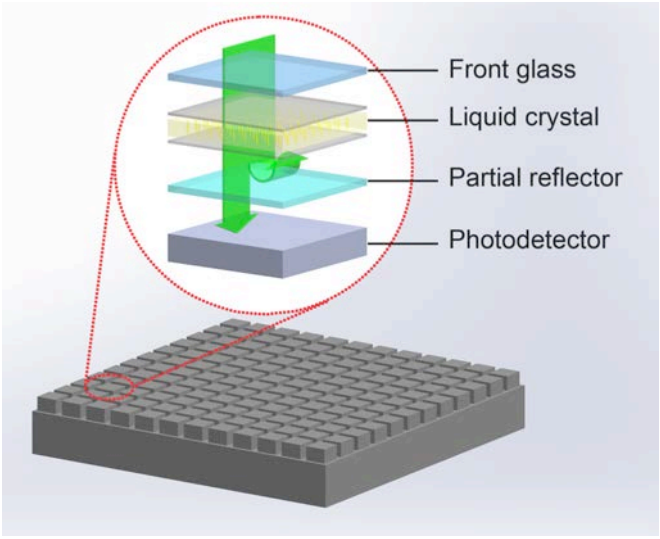

Figure 11: Digital phase conjugation mirror with integration of a photodetector and a phase modulator.

Consider a cooled detector, to reduce the thermal noise, and achieved performance with avalanche photodiodes (APDs) [Aki2010]. A typical measure is the noise equivalent power (NEP), which is in the range of 10^{-18} – 10^{-17} W/Hz$^{1/2}$ for commercially available APDs and photomultiplier tubes (PMTs), but can be as low as approximately 10^{-22} W/Hz$^{1/2}$ single-photon-counting detection of an APD operated at 78 K [Aki2010]. The picture here is that thermal noise dominates. The NEP is the light level required to obtain a SNR=1.

Interestingly, not all wavefront shaping methods can benefit from detector noise improvements. Methods that use interferometry to determine wavefront phase information can operate in the shot-noise limited detection regime by simply using a high power reference beam. Optical phase conjugation methods are almost all interferometry based.

Data transfer from cameras to spatial light modulators is a key limiting factor in experiments where scattering media are dynamic. To this end, a fully integrated camera and spatial light modulator system that is capable of delivering sub-millisecond response time is highly desirable.

3.9. Example Applications and Potential

Some salient examples are listed in this section. The goal is not to provide an exhaustive list but to show by example what is and what may not be possible.

3.9.1. Technological Developments

Dedicated phase conjugation hardware: A dedicated digitally controlled phase conjugation device (Figure 11) that: can perform phase conjugation of an incident wavefront with a response time of < 100 ns, has 1 Gigapixel resolution (pixel size on the order of 1 micrometer); and provides shot-noise limited phase resolution will have high impact. This technology is a prerequisite for significant advancements of a majority of methods and a key enabler for several applications. Achievement of this is likely possible

within a 5 to 10-year timeframe, but requires significant and continued investment of money and effort. Present-day technology can in principle already enable this at a lower pixel resolution (megapixel range) and with a response time in the range of a few ten's of milliseconds.

For a camera to be suitable for DOPC use, high speed and high pixel count are the two primary consideration specifications. Getting near shot noise-limited detection is generally not considered a particular challenge as the wavefront measurement process usually involves the use of interferometry, and the shot noise level detection can be accomplished as long as the reference field is sufficiently strong. The pixel count is currently in the 10-100 megapixel range. The bit depth of the camera is relevant in most applications. During interferometry measurements, the signal we are typically trying to discern is weak and riding on top of a strong DC background (due to the strong reference field). A large bit depth camera ensures that we are able to detect that weak signal. A 16 bit camera is generally used, but we really only care about the last 2-4 bits of our measurements. The high bit count has the unfortunate downside of creating a high data volume download burden from the camera.

A camera that has a high number of pixels is highly desirable. A camera that can output the difference signal is also highly desirable. Such a camera is within the industry's technical ability to implement. If one is to manufacture a camera like this with existing foundries, the intrinsic size of the silicon wafer is likely the current limiting factor. But suppose we use a single wafer to create a camera, and suppose the pixel size is 2 microns. The maximum number of pixels we can fit on the wafer is equal $(30\text{ cm} / 2\text{ microns})^2$ = 23 gigapixels, or roughly 200-500 times the number of pixels in a currently available camera.

An SLM optimized for OPC use should be highly responsive (matching camera speed if possible). The number of phase levels does not have to be large; in fact, an SLM with 4 levels would give a wavefront shaping efficiency that is 80% as good as an SLM with an infinite number of phase levels

Thus far, we have discussed implementing OPC with the combination of a camera and an SLM. An integrated SLM-camera system, where each SLM pixel is built on top of the camera pixel (Figure 10), is a highly desired apparatus that would significantly boost performance and ease-of-use. Such a scheme would eliminate the exacting alignment demanded by the current OPC setup design. It would also greatly ease the task of data transfer from the camera to the SLM, as in this case the data from each camera pixel only needs to travel to the associated SLM pixel.

Path from technology to imaging performance: The technological developments indicated here would be extremely relevant to the stated goals for imaging in tissue. The imaging depth scales roughly as $\left(N_{pixels}\, F\right)^{1/4}$, where F is the refresh rate of the device and N_{pixels} is the number of independently addressable phase pixels. Therefore, an improvement in $N_{pixels}\, F$ by four orders of magnitude will gain one order of magnitude in imaging depth.

3.9.2. Static Scattering Material Properties

The following properties are needed to specify a stationary random scattering medium.

- Scattering mean free path (scattering coefficient)
- Transport mean free path (related to reduced scattering coefficient)
- Wavelength
- Average (effective) refractive index
- Absorption coefficient
- Homogeneity of the scattering properties (e.g., are there voids or gradients in scatterer density)
- Scatterer size and density
- Dispersion/ wavelength dependence of transport properties

3.10. Physical Limits on Phase Coherent Methods in Scattering Media

3.10.1. Physical Limits

In the following we summarize in a graphical way some of the physical limits that must bound the possible parameters where coherent techniques could be applied. The relevant parameters are:

L	Distance at which the target is located from the source or SLM
l_s	Scattering length or mean free path (effective distance over which light is lost from a collimated beam)
l^*	Transport mean free path (scattering mean free path weighted by scattering angle – on the order of 10 l_s for tissue
τ_0	Characteristic scatterer correlation time (time for scatterer to move $\lambda/2$)

Using these parameters we can derive the following parameters.

Thouless time – the average time it takes light to reach the target - $\tau_T = 3\,L^2/cl^*$. This is also a measure of the spread of times over which a short pulse will broaden on its way to the target. (Note that the Thouless time is defined with slightly different numerical prefactors in various references, and the assumption is made here that the medium has refractive index of approximately 1 and is nondispersive.)

An estimate of the **speckle correlation time** – $\tau_{sp} = \tau_0(l^*/L)^2$

The following technical parameters are defined to facilitate presentation of the current status:

1. Processing time - T_p: the time it takes for a phase conjugation system to process a measured field and represent it as a conjugated field. Presently, this is several milliseconds, but could conceivably be reduced to the microsecond range.
2. Guide star radius, for guide star enabled methods. For ultrasound guide stars, this relates to the ultrasound diffraction limit.
3. Guide star efficiency, the probability of a photon that traverses the guide star volume to be "tagged".
4. The number of modes that an imaging/wavefront shaping system can process.
5. The power of the light source. From various considerations, we assume this to be of order 1W.

The physical limits come from the following basic requirements:

1. SNR – the signal needs to be adequate in one correlation time at the target in order to derive correcting fields. This requirement in many practical situations of interest simplifies to "one photon per speckle area per correlation time."
2. Stationarity or "Round Trip Limit" – the scattering medium must remain unchanged between the initial sensing and the delivery of the corrected field.

There are two basic physical scenarios that were discussed:

1. "A spherical cloud", where a source is emitting at the center of such a scattering cloud of radius L. With no absorption, at steady state, the power emitted from the surface of the cloud must be equal to the source power. The number of speckles scales with L^2/λ^2 and the power per speckle drops as λ^2/L^2.

2. "A slab cloud", where the source is on one side and the target on the other side of a scattering medium. Here, some of the light would be reflected off the cloud, the total transmitted power drops as l/L^* and hence the power per speckle scales as $\lambda^2 l^*/L^3$.

Imaging through a scattering medium presents requirements that differ from those for **power delivery**. The ability to deliver power does not imply imaging is possible. Optical phase conjugation and wavefront shaping are essentially methods for setting up a power delivery channel. Imaging could involve:

1. A controllable guidestar, such as an ultrasound focus - Thus far, no suitable guidestars have been created in gaseous media, however microwave heating and other approaches may be plausible.
2. The optical memory effect - This means the scattering medium should be no thicker than about 100 wavelengths.
3. Ballistic or few-scattered photons - This only works in the boundary layer of the medium, typically up to l^*.
4. Acousto-optics - In this case, one uses the light to excite acoustic waves that are subsequently imaged assuming they propagate ballistically. This modality requires a dense medium such as water or biological tissue for ultrasound propagation and cannot work in air or aerosol media.
5. Transmission matrix data - This can only be obtained by an invasive procedure and is usable only within the correlation time.
6. Bootstrap imaging - Obtaining microscopic data on scatterer positions from backscattered light, which is subsequently used to calculate the transmission matrix numerically. There has be no experimental confirmation yet that this is possible.

7. Diffusive optical tomography (with time-dependence) - This method allows in principle for imaging at any depth, however, the resolution is dictated by the physics of the model, the measured data set, and the computational imaging problem. In thick scattering materials, the resolution has been limited to about depth/4, as the radiative transfer equation that governs the propagation of diffusive light exponentially suppresses the waves that carry high-resolution information. Extending the resolution/depth ratio by more than about a factor of 2 will be a challenge.

Figure 12 and Figure 13 plot the appropriate constraints on a map of τ versus range. None of the limits are absolute, e.g., the SNR limit is taken to be SNR=1, whereas in some cases a higher SNR may be needed or a lower SNR may be acceptable. However, the limits presented represent a cusp in the difficulty of retrieving information from the system. All graphs were made under the "spherical cloud" assumptions, which are the most prevalent ones.

Under the assumptions used, we find that the SNR requirement of "one photon per speckle" can be expressed as $\frac{P_{source}}{\hbar\omega}\frac{\lambda^2}{16\,\pi\,R^2}\,\tau_{sp} > 1$, which simplifies to

$$\frac{P_{source}}{\hbar\omega}\frac{\lambda^2\tau_0(\ell^*)^2}{16\,\pi\,R^4} > 1. \tag{33}$$

The time-domain constraint is given by the fact that the phase conjugation plus propagation processes must have finished before the medium decorrelates, i.e., the speckle correlation time must be larger than the Thouless time (the time for half the photons to traverse the medium) plus the electronic processing time, giving

$$\tau_{sp} > \tau_T + T_p \tag{34}$$

$$\tau_0 (l^*/L)^2 > \frac{3\,L^2}{c l^*} + T_p. \qquad (35)$$

Finally, the absorption becomes significant at the characteristic length on which photons are absorbed. Figure 12 presents this information for clouds and Figure 13 for tissue. In Figure 12, for biological tissue (transport mean free path of 1 mm), we find that the SNR limit and the roundtrip limit (assuming a 10 microsecond processing time) lie close together and the usable depth for OPC is several cm. Assuming correlation times on the scale of a second (which may be appropriate for tissues with no significant blood flow), it seems that loss of SNR due to absorption is the final limit. The dashed red circle indicates the approximate range of current experiments.

Figure 12 shows that in clouds and dense fog (l_s = 10 m; l^* = 100 m), the round trip limit with an assumed electronic processing time of 10 microseconds confines the range to a few hundred meters. A more important problem is the loss of SNR, which even for slowly moving droplets does not allow a range of more than about 100 m. In a pure phase conjugation setup, one may, however, trade SNR for pixel number, allowing extension of the range by decades. Imaging typically has more stringent SNR requirements than pure phase conjugation. Opportunities for coherent control are very good in tissue, due to the availability of good ultrasound guide stars, the low absorption in the infrared and the surprisingly long correlation times. However, gaseous media present more challenges, due to: the lack of a demonstrated guidestar approach; the potentially large size of the media, making the power per speckle low; and the expected short correlation time of such media.

Optical imaging methods using incoherent detection of short pulses were shown to be useful in an "around the corner" imaging scenario and in imaging through slabs of dense scattering materials. These methods have the advantage of being relatively insensitive to perturbations in the environment and can image through highly dynamic media, but have suffered from low resolution.

From Figure 12, for clouds and fog, wave front shaping and phase conjugation have only limited potential to extend the depth range of

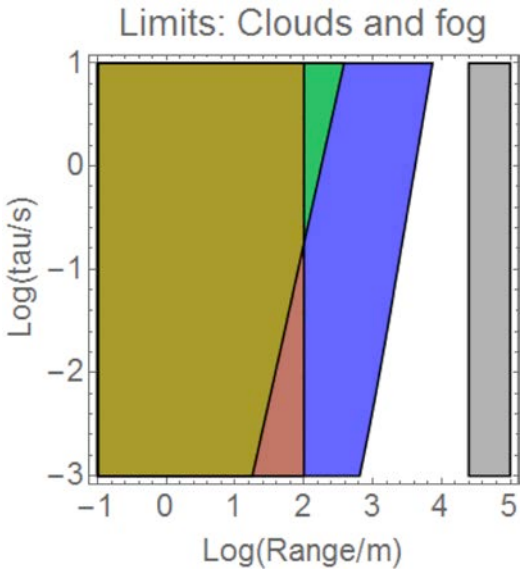

Figure 12: Physical limits on the use of optical phase conjugation in atmospheric media such as clouds and fog. The boundaries are relative to a reference medium with a scattering coefficient of 0.1/m (scattering mean free path of 10 m) and a reduced scattering coefficient of 0.01/m (transport mean free path of 100 m).

Horizontal axis: The range in meters (on a base-10 logarithmic scale)

Vertical axis: The correlation time of the medium. This correlation time depends on the velocity of motion of the scatterers and can be very different for media of different types or even between different types of fog.

Orange (on some systems olive) area: Ballistic zone, up to one transport mean free path in depth. In the ballistic zone imaging by optical coherence tomography or related "gated" imaging methods is typically possible. In the ballistic zone speckle is partially developed. To the right of this area we have fully developed speckle.

Green area: Zone of opportunity for phase conjugation/ wave front shaping methods. In this area the best possible signal to noise (based on physical limits, not current technology) is good enough to successfully perform optical phase conjugation.

Blue area: Round trip allowed zone. In this zone, the round trip time of a light signal (including an electronic processing time of 10 microseconds) is shorter than the correlation time of the medium.

White area: No realistic opportunity for phase conjugation based methods as the round trip time (+ electronic processing time) for light exceeds the correlation time of the medium.

Grey area: In this area absorption, even for the best choice of wavelength, is too strong to achieve imaging or light delivery through phase conjugation.

imaging methods. Phase conjugation can extend the depth range of power/signal delivery at depths where conventional imaging is still possible but light delivery becomes inefficient.

In Figure 13 we show the physical limits of optical phase conjugation in tissue. The figure contains the same information as Figure 12. In tissue the range accessible to present methods of focusing and imaging light is less than 1 mm, whereas optical phase conjugation is predicted to be feasible up to a depth of centimeters in tissue with a long correlation length.

Method by which the figures in this section were determined: The detailed equations for the specific lines in Figure 12 are as follows. The line that marks the edge of the ballistic zone is $L = l^* = 100\,\mathrm{m}$. The line that marks SNR $= 1$ for phase conjugation (SNR limit) is given by (33), with the photon flux corresponding to a power of 1W, $P_o/(\hbar\omega) = 1.6\,10^{19}/s$. The line that marks the round trip time limit is given by (35), with $T_p = 10\,\mu s$.

The detailed equations for the specific lines in Figure 13 are as follows: The line that marks the edge of the ballistic zone is $L = l^* = 1$ mm. The line that marks SNR $= 1$ for phase conjugation (SNR limit) is given by (33), with the photon flux corresponding to a power of 1W, $P_o/(\hbar\omega) = 1.6\,10^{19}/s$. The line that marks the round trip time limit is given by (35), with $T_p = 10\,\mu s$.

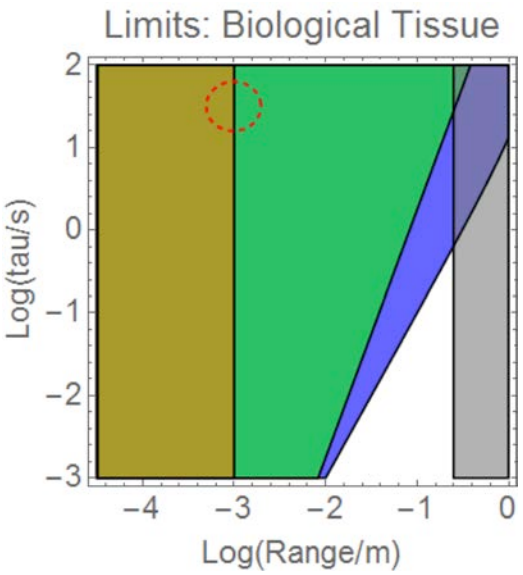

Figure 13: Limits of optical phase conjugation in tissue in the parameter space of correlation time and depth range. The reference medium is typical of soft biological tissue with a scattering mean free path of 0.1 mm and a transport mean free path of 1 mm. The absorption coefficient is assumed to be 0.004/mm, which is applicable to the near-infrared region. Areas and axes as in Figure 3. The red dashed circle represents current achievements. Note the substantial increase in distance that is possible before propagation time or absorption limits. The line and color codes are the same as Figure 12.

3.10.2. Technological Challenges

Challenges motivate new technology that include:

1. Focusing - The development of methods to facilitate a λ /2 focus deep inside scattering media, or even better in the near field.
2. Control of modes - The experimental control of many optical modes (up to 100,000 modes currently).
3. Transmission matrix - The study of transmission matrices with significantly higher number of modes than previously considered practical (>1000).
4. Imaging - The idea of combining the optical memory effect and phase retrieval approaches to image a target behind an opaque screen.

Specific needs in new technologies are:

1. Integration of the SLM with a camera will circumvent the limiting data transfer between the SLM and the camera.

2. Much higher pixel count (upwards of 100 megapixels) is desired as it impacts on the amount of wavefront details we can render.
3. More phase levels is not a priority, in comparison with a larger pixel count. Even with binary phase, wavefront shaping can be performed effectively. Alternately, wavefront shaping can be performed with reasonable effectiveness with simple on-off amplitude control.
4. Faster response spatial light modulators are desirable. This will likely require solutions beyond liquid crystals.
5. Alternate methods for mixed modality guidestars are desirable.

Opportunities on both the physical and computational fronts highlight the role of signal processing technology.

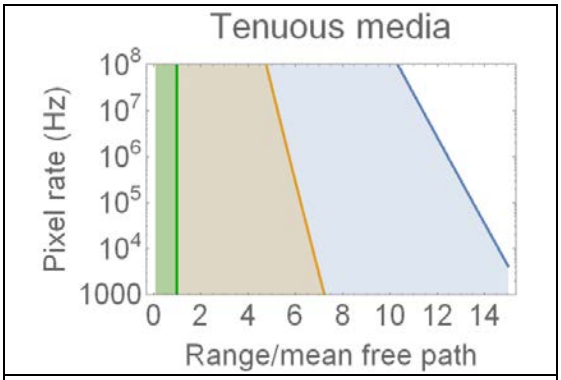

Figure 14: Model-based physical limits for diffraction-limited ballistic imaging methods in tenuous scattering media. The vertical logarithmic axis shows the theoretical best pixel rate that can be obtained with SNR of 1 in the reference condition, versus range. Green: Reference method. Brown: Digital contrast enhancement. Blue: Gated imaging methods. The area where each method has SNR>1 is shaded in the corresponding color.

3.11. Physical Limits on Incoherent Imaging Methods in Scattering Media

In this section, formulas and graphs are given that outline the physical limits of incoherent imaging methods in tenuous scattering media such as fog, turbid water and snow. First we develop a straightforward model to predict the physical limits to the signal to noise ratio (SNR) that can be obtained using several relevant methods:

A. Traditional imaging. The reference method, direct observation of images;
B. Digital contrast enhancement of high-dynamic range images;
C. Gated imaging methods (OCT and time-gated imaging) with digital processing;
D. Time-gated diffuse tomography methods.

It should be noted here that methods A through C can operate at any resolution of choice; one could use them to zoom in on a high-resolution license plate at long range or "zoom out" to scan an area. Method D operates at a low resolution of about depth/5, and exponentially loses signal to noise at higher depth to resolution ratios.

The performance of any method is given in terms of the maximum pixel rate at a SNR of 1. For useful imaging in most scenarios 10^5 pixels/second with a SNR of 1 is needed, e.g., to obtain a 10 Hz frame rate of small 100x100 pixel frames. In all reference scenarios we assume a light source of 1W (10^{19} photons/s) and to calculate the theoretical best performance we also assume the best possible wavelength range is chosen (e.g., FLIR for imaging through fog). Moreover, the reference target is a Lambertian target with 100% reflectivity contrast (e.g., black text on white paper). Mirror or corner cube targets at a specific orientation are easier to image but such cases are unrealistic in real-world scenarios.

3.11.1. General Case: Incoherent Imaging in Tenuous Media

Reference method: The reference method (direct imaging) can resolve objects up to about 1 mean free path in depth. Beyond this the signal to background ratio drops below 1. The area where the reference method has a SNR>1 is shown as green in Figure 14 - Figure 16.

Digital contrast enhancement: In many cases a digital camera can capture a high-dynamic range image, which can then be digitally processed to increase the contrast (by e.g., Fourier filtering) and thereby suppress the scattered light. This type of contrast enhancement depends somewhat on specific assumptions about the scattering medium, for instance the scatterer density needs to be homogeneous or known. In case of an inhomogeneous scatterer density uncontrollable artefacts may appear in the image.

Alternately, this analysis is also valid for interferometry-based image detection. This type of imaging/detection method can reach shot-noise level sensitivity by employing a sufficiently strong reference beam for interference. Moreover, the process automatically select for detection only light field component that shares the same coherence properties as the reference beam – thereby allow the user to suppress scatter light in the detection process.

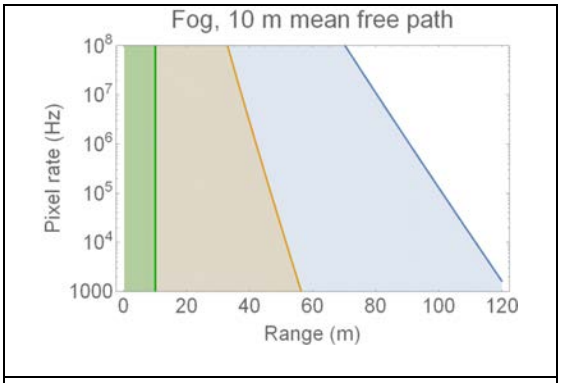

Figure 15: Model-based physical limit of the pixel rate for diffraction-limited ballistic imaging methods in dense fog with a mean free path of 10 m. The collection optic radius is assumed to be 25 cm. Green: Reference method. Brown: Digital contrast enhancement. Blue: Gated imaging methods.

The best possible performance of such a procedure can be estimated as follows: the source flux is F (photons per second), and the number of pixels measured per second (pixel rate) is p. When light is reflected by a Lambertian surface object it spreads out over all angles with an intensity

$$I_{lambertian}(R,\theta) = \frac{P_{reflected}\, cos(\theta)}{\pi\, R^2}, \qquad (36)$$

where θ is the angle between the direction of propagation and the surface normal, $P_{reflected}$ is the total reflected power and R is the distance from the Lambertian reflecting surface. As a result, the geometrical probability to hit the detector (assuming a non-scattering environment and a surface oriented normal to the line of sight to the detector so that $\cos(\theta) = 1$) is $\pi\, r_{detector}^2/(\pi L^2)$. The extinction coefficient is $\mu_{ext} = \mu_s + \mu_a$, which leads to an additional round trip loss for ballistic photons of $\exp(-2\,\mu_{ext} L)$.

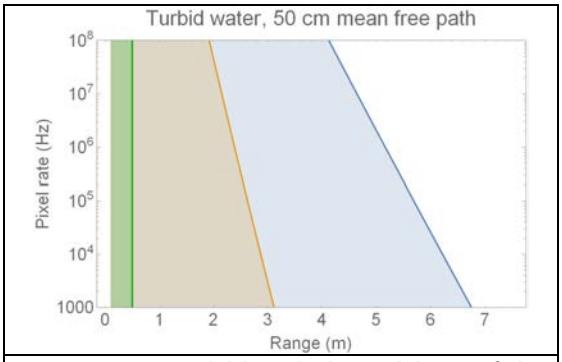

Figure 16: Model-based physical limit of the pixel rate for diffraction-limited ballistic imaging methods in turbid water with a mean free path of 0.5 m. The collection optic radius is assumed to be 5 cm. Green: Reference method. Brown: Digital contrast enhancement. Blue: Gated imaging methods.

The detector is assumed to be ideal. The illumination is assumed to be provided by a beam aimed at the object. This beam will be scattered at a depth of about 1 transport mean free path in the medium (l^*), and the detector will pick up a number of scattered photons of order $F\, r_{detector}^2/(pl^{*2})$, and even for an ideal detector there will be shot noise at a level $\sqrt{F\, r_{detector}^2/(pl^{*2})}$, hence, assuming only the inevitable shot noise is present,

$$SNR_{contrastenh} = \left(\frac{r_{detector}^2 F}{L^2 p}\right) exp(-2\,\mu_{ext} L)\, \left(F\, r_{detector}^2 \frac{\mu_s'^2}{p}\right)^{-1/2}. \qquad (37)$$

As a result, the SNR is smaller than 1 above the maximum pixel rate

$$p_{max;ce} = \frac{r_{detector}^2 F}{e^4 \mu_{ext}^2{}^L \, L^4 \mu_s'^2}. \quad (38)$$

In Figure 14 - Figure 16 we have shaded the area where $\mathrm{SNR}_{\mathrm{contrastenh}}$ exceeds 1 as brown.

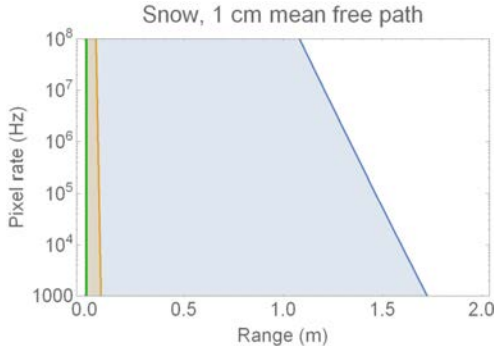

Figure 17: Model-based physical limits for imaging methods in snow with a mean free path of 0.01 m. For the curves drawn here, the collection optic is assumed to be in contact with the medium. For standoff operation one expects a pixel rate that is reduced by a factor of about 10000 with respect to the curves shown here. Green: Reference method. Brown: Digital contrast enhancement. Blue: Diffuse tomography methods with a target resolution of 20 cm.

Gated imaging methods: In gated imaging methods the light is time gated so that any scattered photons (which arrive at the detector at the wrong time) are rejected. Streak cameras and other fast detectors can be used to implement time gating. Alternately, this process can be easily accomplished through the use of low coherence (temporal) light and interferometry. The main physical limitation is that at great depth not even a single photon may be detected within the integration time.

The signal to noise ratio is $SNR_{gated} = F \; \varepsilon \; r \, e^{-2\mu_{ext}{}^L} T$; here F is the source photon flux, ε the detection efficiency (taken here as 1 for an ideal detector), the scattering coefficient is μ and $T = 1/p$ is the time available to acquire a pixel. For the Lambertian reflector that is our reference object, the effective reflectivity is $R=r_{detector}^2/(L^2)$. As a result the theoretical maximum pixel rate at which SNR>1 is given by

$$p_{max;gated} = \frac{r_{detector}^2 F}{e^2 \, \mu_{ext}{}^L \, L^2}. \quad (39)$$

In Figure 14 we show the general physical limits of ballistic imaging methods (Contrast enhancement and gated imaging) on a normalized scale. For useful real-time imaging the pixel rate must be of order 10^5 pixels/second, e.g. 10 frames per second of 100x100 pixels. At such rates contrast enhancement methods are limited to about 6 mean free paths while gated imaging methods have the potential to reach almost 14 mean free paths.

Method by which the figures in this section were determined: The detailed equations for the specific lines in Figure 14 are as follows. The green line that marks the edge of where the reference method has good contrast is simply given by $L = l^*$. The brown line that marks the edge of the useful range of digital contrast enhancement is given by $SNR_{contrastenh} = 1$, with $SNR_{contrastenh}$ given by (37), and assuming the detector radius is very large, $r_{detector} = l^*$, and the photon flux corresponds to a power of 1 W, $F = 10^{19}/s$. The blue line that marks the edge of usefulness of gated imaging methods is given by (39), with the same parameters.

3.11.2. Imaging in Fog

Our reference situation for fog is a dense fog with a transport mean free path (in the FLIR band) of $l^* = 10$ m. We obtain the graph of Figure 15, assuming a collection optic with a radius of $r_{detector} = 0.25$ m (diameter of 0.5 m, e.g., a large Fresnel lens). We assume an efficient and noiseless detector, which presently is not available in the FLIR region. It is at the physical limit of gated imaging methods to

obtain imaging at the desired speed and SNR at a depth of 100 m in the reference situation, which is 10 times the current state of the art.

Method by which the figures in this section were determined: The detailed equations for the specific lines in Figure 15 are as follows: The green line that marks the edge of where the reference method has good contrast is simply given by $L = l^* = 10$ m. The brown line that marks the edge of the useful range of digital contrast enhancement is given by $SNR_{contrastenh} = 1$, with $SNR_{contrastenh}$ given by (37), and the photon flux corresponds to a power of 1 W, $F = 10^{19}/s$. The blue line that marks the edge of usefulness of gated imaging methods is given by (39), with the same parameters.

3.11.3. Imaging in Turbid Water

The situation for imaging in turbid water is depicted in Figure 16. In the reference situation we assume a mean free path of $l^* = 0.5$ m, and a detector radius $r_{detector} = 0.05$ m, all other parameters as in the previous figure. Except for the scale, the situation is very similar to that of dense fog. A range of about 5 m should be achievable for blue-green light where the absorption is low.

3.11.4. Imaging in Snow

The reference scenario for imaging in snow is an imaging method that can find a buried object or person under 1 m of snow with a mean free path of 1 cm. In this scenario image enhancement and even gated imaging methods are of comparatively little value as they can reach at best about 10 mean free paths. At these depths, and with the comparatively low resolution needed for the task, computational diffuse tomography methods can obtain good signal to noise and sufficient resolution. The theoretical performance resulting from our model is shown in Figure 17. It shows that even at depths exceeding 1m a useful imaging rate can be obtained, taking into account that a pixel radius of 0.1 m (resolution of about 0.2 m) should be acceptable. As explained below, there is even headroom for stand-off operation, which is possible at the cost of drastically reducing the achievable pixel rate.

In this class of imaging method, an upper bound to the signal is found from considering the total number of photons that interact with the object, followed by back-propagation of the information to the detectors. The number of photons that interact with a resolution area on the object is given by the size of this area, πr_{res}^2, multiplied by the diffuse photon flux density inside the medium at depth L, which is $I(L) = \left(\frac{F}{p}\right)\left(\frac{1}{\mu_s' L}\right)\left(\frac{1}{L^2}\right)$. We assume here negligible absorption. The photons that interacted with the object propagate back to the detector side through the medium. Here, the Fourier components that carry the image information are attenuated. The information to reconstruct an image at a resolution corresponding to spot radius r_{res} is attenuated by a factor $\exp\left[-\frac{L}{2\, r_{res}}\right]$. Assuming any detection background can be sufficiently removed by using time gating or fluorescence, the number of signal photons available for detection outside the medium is

$$n_{detectable} = \left(\frac{F}{p}\right)\left(\frac{\pi r_{res}^2}{\mu_s' L^3}\right)\exp\left[-\frac{L}{2\, r_{res}}\right]. \quad (40)$$

In this ideal case the theoretical SNR is given by $SNR_{Diffuse} = n_{detectable}^{1/2}$, and the maximum pixel rate is given by

$$p_{max;diffuse} = \frac{\pi\, r_{res}^2 F}{\frac{L}{e^{2r_{res}}}\, L^3 \mu_s'}. \quad (41)$$

In case of detection at a standoff distance $L_{standoff}$ from the medium, the detection efficiency is reduced by a factor $r_{det}^2 / L_{standoff}^2$. Assuming a standoff distance of 100 m and a 25 cm optic radius, the detection efficiency is 6×10^{-6}. The maximum achievable pixel rate is reduced by the same factor.

Therefore we conclude that even with standoff operation a useful imaging rate can in principle be achieved in the reference situation. The influence of medium inhomogeneity such as variation in the packing density of snow is not taken into account here and is a serious challenge for diffuse tomography methods.

Method by which the figures in this section were determined: The detailed equations for the specific lines in Figure 17 are as follows. The green line that marks the edge of where the reference method has good contrast is simply given by $L = l^* = 1$ cm. The brown line that marks the edge of the useful range of digital contrast enhancement is given by $SNR_{contrastenh} = 1$, with $SNR_{contrastenh}$ given by (37), and assuming the detector radius is very large, $r_{detector} = 0.1$ m, and the photon flux corresponds to a power of 1 W, $F = 10^{19}/s$. The blue line that marks the edge of usefulness of gated imaging methods is given by (41), with $r_{res} = 0.1$ m, and all other parameters as in the other curves.

4. Conclusion

This investigation leads to the following positions with regard to opportunities to penetrate more scatter using light. A program to develop fundamentally new methods to transfer information through highly scattering media will allow an increase in the range of more than an order of magnitude. Rather than exclusively addressing a specific type of scattering media, efforts could encompass several media of practical relevance ranging from dense fog to biological tissue, thereby addressing issues of fundamental and broad importance to facilitate a paradigm shift. Success will permit high resolution imaging throughout large portions of the human body, the attainment of tactical information through heavily scattering aerosols (e.g., fog, dust, and smoke), provide opportunities to peer through turbid water, and enable information to be sent through ice and snow, all in ways that to date were thought not to be achievable but are in fact within reach, based on basic physical considerations.

4.1. Research Concentration Areas

A critical core of methods and technology are to be developed for imaging, sensing, communication and energy delivery through media that scatter light. Detailed and quantitative objectives depend on the type of medium under consideration, but consistently aim to extend the penetration depth by an order of magnitude with respect to the current state of the art while retaining task-specific useful resolution, contrast and speed. While challenging and requiring technological and conceptual breakthroughs, these objectives are in principle possible and will not violate physical limits imposed by, for example, detector signal-to-noise ratio, causality or information theory [2.12, 6.1]. Imaging is usually the most demanding application, as it may require high-resolution spatial information from a field of view as well as scanning, which is not always possible. Sensing, communication and energy delivery may be simpler in terms of spatial requirements, but they involve stringent issues related to response time, efficiency and spectral response.

4.2. Key Physical Domains of Interest

For each of the domains we present a reference scenario, with parameters that are typical real-life situations where the ability to view through scatter drastically improves safety or capabilities. We assume reference parameters, as the density of media can vary naturally over large bandwidths. It is to be expected that imaging performance scales more or less linearly with the mean free path, i.e., when the mean free path doubles one can expect roughly a doubling of the useful range. Graphs and calculations

demonstrating that the set goals are within the range of physical possibilities, but close to its edge, support the cases.

- **Tissue**

Imaging and delivery of optical energy through centimeters of human tissue is needed in order to optically locate, recognize and affect critical features such as tumors, lesions and foreign objects in the body, and to extend the reach of brain imaging in a manner that will have profound impact on neuroscience.

As a reference system we assume tissue with a scattering mean free path of 0.1 mm and a transport mean free path of 1 mm. The state of the art in such tissues is that imaging is possible to a depth of about 1 mm. The specific goals in this reference situation are:

- Penetration depth of 10 mm or more - ten times the state of the art [For acoustic assisted optical focusing in dead tissue, the current state of the art is able to focus to a point of ~30 microns diameter at a depth of 2.5 mm at a wavelength of 530 nm with: ~10^4 controllable optical modes, an ultrasound frequency of 50 MHz, and an exposure time is of ~100 ms. The exposure time is limited by the decorrelation time, about 30 ms for 2 mm of tissue.]
- Resolution on the cellular scale, on the order of 10 micron, enabling the recognition of larger cells
- Intrinsic contrast or biocompatible contrast agents suitable for use in living tissue
- More than 10^4 pixels/second imaging speed at SNR>1 when imaging a biological object at the greatest depth, but even 10^2 pixels/second will be useful in some situations

- **Fog and aerosols**

Vision, communication and sensing through heavy fog or snowstorms is sought, extending the typical range from about 10 meters to 100 meters for safe driving or the landing of (autonomous) vehicles. We assume a reference situation where a dense fog has a 10 m mean free path in the FLIR spectral region. State of the art in this case is FLIR imaging, with a range of one mean free path. The reference task is recognition of an object (black text on white paper) at a resolution of 10 cm and a range of 100m. The specific goals are:

- Penetration depth of 100 m, ten times the state of the art
- A spatial resolution that would allow discernment of 10 cm objects at 100 m
- More than 10^4 pixels/second imaging speed at SNR>1

- **Turbid water**

Imaging in order to locate objects at a range of distances in turbid (e.g., polluted) water will facilitate rescue operations, the identification of foreign objects, and the monitoring of water chemistry using light. Our reference system is water containing scatterers or bubbles leading to a mean free path of 50 cm. State of the art in this case is imaging down to about two mean free paths using integral imaging with contrast enhancement. The specific goals are:

- Penetration depth of more than ten times the mean-free path
- Resolution of 1 cm at a range of 5 m
- More than 10^4 pixels/second imaging speed at SNR>1 when imaging a Lambertian object (e.g., black text on white paper) at a depth of 10 mean free paths

- **Snow and sea ice**

Vision through snow and sea ice will be of great value in rescue operations**.** Avalanche snow has a mean-free-path of a few mm. Low resolution methods that can remotely detect a person buried under 1 m of snow (several hundred mean free paths) would change the way search and rescue

operations are conducted. The reference scenario assumes snow with a scattering mean free path of 1 cm and negligible absorption, and a high-contrast target (bright ski wear). The specific goals are:

- Penetration depth of 1 m, ten times the state of the art
- Resolution of better than 20 cm at a depth of 1 m
- More than 10^4 pixels/second imaging speed at SNR>1 when imaging a Lambertian object (e.g., black text on white paper) at 1 m depth

4.3. Scientific and Technological Domains

To enable the application spaces described in Section D, revolutionary progress in the following domains is sought.

- **Scattering medium characterization**
  - Experimental data describing relevant (dynamic) scattering media
  - Basic physical requirements for devices and the limits on resulting imaging and communication systems
  - Modeling and analysis for coherent methods in dynamic scattering media
  - Statistical and numerical methods for medium description that provide for data interpretation

- **Device development**
  - Higher resolution and faster wavefront modulators [Current technology offers HDTV resolution at 60 Hz, and faster devices at significantly lower resolution (e.g., 2000 elements at ~50 kHz). New devices should offer $NF>10^9$, with N controllable elements and a refresh rate F.]
  - Integration of modulators with solid state cameras, e.g., for ultrasound-assisted methods
  - Solid-state cameras that combine high speed with high pixel count
  - Sources with suitable characteristics such as coherence, spatial and spectral scanning, and wavelength

- **System development**
  - Imaging methods with the potential for wavelength scale resolution and biochemical specificity
  - Coherent and incoherent methods, including those with mixed modalities, for communication, sensing and imaging in rapidly changing media
  - Methods to inject illumination light deeper into scattering media, including the improvement of ultrasound guidestars and methods to use their signal, and the development of new and more efficient guidestar mechanism

5. Acknowledgement

We thank the following people for their very valuable input at a workshop to discuss the issues that were held in Arlington, VA, March 3-4, 2015: Joseph Altepeter; Berberian & Company; Ravindra Athale, Office of Naval Research; Yaron Bromberg, Yale University; Hui Cao, Yale University; Sylvain Gigan, Université Pierre et Marie Curie; Clifton Haider, Mayo Clinic; Chia Wei Hsu, Yale University; Ori Katz, Institut Langevin, LKB; Prem Kumar, DARPA/DSO; Joseph Mait, US Army Research Laboratory; Jerome Mertz, Boston University; Predrag Milojkovic, DARPA; Rafael Piestun, University

of Colorado at Boulder; Ramesh Raskar, MIT Media Lab; Margaret Rowland, Strategic Analysis, Inc.; Guy Satat, MIT; A. Douglas Stone, Yale University; John Sura, DARPA/DSO; Ivo Vellekoop, University of Twente; Lihong Wang, Washington University in St. Louis.

6. References

[Abr1978] N. Abramson, "Single pulse light-in-flight recording by holography," *Opt. Lett.* **3**, 121,1978.
[Akb2013] D. Akbulut, *Measurements of Strong Correlations in the Transport of Light Through Strongly Scattering Materials*, Ph.D. thesis, University of Twente, 2013.
[Ake2011] G. Akemann, J. Baik, and P. di Francesco, (Eds.), *The Oxford Handbook of Random Matrix Theory*, Oxford University Press, 2011.
[Aki2010] M. Akiba, K. Tsujino, and M. Sasaki, *Opt. Lett.* **35**, 2621, 2010.
[Akk2007] E. Akkermans and G. Montambaux, *Mesoscopic Physics of Electrons and Photons*, Cambridge University Press, 2007.
[Ant2014] J. Antonello, T. van Werkhoven, M. Verhaegen, H. H. Truong, C. U. Keller, and H. C. Gerritsen, "Optimization-based wavefront sensorless adaptive optics for multiphoton microscopy," *Journal of the Optical Society of America A*, **31**, 1337, 2014.
[Arr1999] S. R. Arridge, "Optical tomography in medical imaging," *Inverse Probl.* **15**, R41–R93 (1999).
[Aul2011] J. Aulbach, B. Gjonaj, P. M. Johnson, A. P. Mosk, and A. Lagendijk, "Control of light transmission through opaque scattering media in space and time," *Phys. Rev. Lett.*, **106**, 103901:1 -4, 2011.
[Bal1997] B. Ballou, G. W. Fisher, T. R. Hakala, and D. L. Farkas, "Tumor detection and visualization using cyanine fluorochrome-labeled antibodies," Biotechnol. Prog. **13**, 649–658 (1997).
[Bar1991] H. Baranger, D. DiVincenzo, R. Jalabert, and A. D. Stone, "Classical and quantum ballistic-transport anomalies in microjunctions," *Phys. Rev. B,* **44**, 10637-10675, 1991.
[Bar2008] Ke, San-Huang, Weitao Yang, and Harold U. Baranger. "Quantum-interference-controlled molecular electronics." *Nano letters*, **8**, 3257-3261, 2008.
[Bea1976] K. V. Beard, "Terminal velocity and shape of cloud and precipitation drops aloft," *J. Atmos. Sci.,* **33,** 851–864, 1976.
[Bec2001] A. Becker, C. Hessenius, K. Licha, B. Ebert, U. Sukowski, W. Semmler, B. Wiedenmann, and C. Grotzinger, "Receptor-targeted optical imaging of tumors with near-infrared fluorescent ligands," *Nature Biotech.* **19**, 327–331 (2001).
[Bee1997] C. W. J. Beenakker, "Random-matrix theory of quantum transport," *Rev. Mod. Phys.***, 69**, 731, 1997.
[Bei2011] F. van Beijnum, E. G. van Putten, A. Lagendijk, and A. P. Mosk, "Frequency bandwidth of light focussed through turbid media," *Opt. Lett.*, **36**, 373–375, 2011.
[Ben2015] B. Z. Bentz, A. V. Chavan, D. Lin, E. H. R. Tsai, and K. J. Webb, "Fabrication and application of heterogeneous printed mouse phantoms for whole animal optical imaging", *Appl. Opt*., accepted, 2015.
[Ber1989] R. Berkovits, M. Kaveh, and S. Feng, "Memory effect of waves in disordered systems: A real-space approach," *Phys. Rev. B*, **40**, 737–740, 1989.
[Bes1950] A. C. Best, "Empirical formulae for the terminal velocity of water drops falling through the atmosphere," Q. J. Roy. *Meteor. Soc*., **76**, 302–311, 1950.
[Ber2000] B. J. Berne and R. Pecora, *Dynamic Light Scattering: With Applications to Chemistry, Biology, and Physics*, 2000.
[Ber2005] J. Bertolotti, S. Gottardo, D. S. Wiersma, M. Ghulinyan, and L. Pavesi, "Optical necklace states in Anderson localized 1D systems," *Phys. Rev. Lett.,* **94**, 113903, 2005.
[Ber2012] J. Bertolotti, E. G. van Putten, C. Blum, A. Lagendijk, W. L. Vos, and A. P. Mosk, "Non-invasive imaging through opaque scattering layers," *Nature***, 491**, 232-234, 2012.
[Bir2010] M. D. Birowosuto, S. E. Skipetrov, W. L. Vos, and A. P. Mosk, "Observation of spatial fluctuations of the local density of states in random media," *Phys. Rev. Lett.*, **105**, 013904, 2010.
[Boa1995] D. A. Boas, L. E. Campbell, and A. G. Yodh, "Scattering and imaging with diffusing temporal field correlations," *Phys. Rev. Lett.* **75**, 1855-1858, 1995.
[Boa2012] D. A. Boas, C. Pitri, and N. Ramanujam *(Eds.), Handbook of biomedical optics*, CRC Press, Boca Raton, Fl, 2012.
[Boo2007] M. J. Booth, "Adaptive optics in microscopy," *Phil. Trans. R. Soc. A: Math., Phys. Eng. Sc.,* **365**, 2829–

2843, 2007.
[Boo2012] M. J. Booth, D. Débarre, and A. Jesacher, “Adaptive optics for biomedical microscopy,” *Opt. Photon. News*, **23, 22**, 2012.
[Boo2014] M. J. Booth, “Adaptive optical microscopy: the ongoing quest for a perfect image,” *Light Sci Appl.*, **3**, e165, 2014.
[Bov2007] G. Boverman, Q. Fang, S. A. Carp, E. L. Miller, D. H. Brooks, J. Selb, R. H. Moore, D. B. Kopans, and D. A. Boas, “Spatio-temporal imaging of the hemoglobin in the compressed breast with diffuse optical tomography,” *Phys. Med. Biol.* **52**, 3619–3641 (2007).
[Can2006] E. J. Candès, J. K. Romberg, and T. Tao, “Stable signal recovery from incomplete and inaccurate measurements,” *Comm. Pure Appl. Math*., **59**, 1207-1223, 2006.
[Can2008] E. J. Candès and M. Wakin, “An introduction to compressive sampling,” *IEEE Signal Processing Magazine*, **25**, 21-30, 2008.
[Car2009] I. Carron, *Wavefront Coding for Random Lens Imagers*, NuitBlanche Compressive Sensing Blog, http://nuit-blanche.blogspot.nl/2009/10/cs-wavefront-coding-for-random-lens.html, retrieved August 2013, 2009.
[Cha2013] T. Chaigne, O. Katz, A. C. Boccara, M. Fink, E. Bossy, and S. Gigan, “Controlling light in scattering media non-invasively using the photoacoustic transmission matrix,” *Nature Photon.***, 8**, 58-64, 2013.
[Che2000] K. Chen, L. T. Perelman, Q. Zhang, R. R. Dasari, and M. S. Feld, “Optical computed tomography in a turbid medium using early arriving photons,” *Journal of Biomedical Optics***, 5**, 144, 2000.
[Che2014] Y. Chen, J. A. Newman, and K. J. Webb, “Circular Bessel statistics - derivation and application to wave propagation in random media,” *J. Opt. Soc. Am. A*, **31**, 2744-2752, 2014.
[Cho2011] Y. D. Chong and A. D. Stone, “Hidden black: Coherent enhancement of absorption in strongly scattering media,” *Phys. Rev. Lett.*, **107**, 163901, 2011.
[Choi2011a] W. Choi, A. P. Mosk, Q. - H. Park, and W. Choi, “Transmission eigenchannels in a disordered medium,” *Phys. Rev. B*, **83**, 134207: 1-6, 2011.
[Cho2012] Y. Choi, C. Yoon, M. Kim, T. D. Yang, C. Fang-Yen, R. R. Dasari, K.J. Lee, and W. Choi, “Scanner-free and wide-field endoscopic imaging by using a single multimode optical fiber,” *Phys. Rev. Lett.*, **109**, 203901, 2012.
[Cit1934] P. H. van Cittert, Die wahrscheinliche Schwingungsverteilung in Einer von Einer Lichtquelle Direkt Oder Mittels Einer Linse Beleuchteten Ebene, *Physica* **1**, 201-210, 1934.
[Ciz2010] T. Čižmár, M. Mazilu, and K. Dholakia, “In situ wavefront correction and its application to micromanipulation,” *Nature Photon.*, **4**, 388-394, 2010.
[Ciz2011] T. Čižmár and K. Dholakia, “Shaping the light transmission through a multimode optical fibre: complex transformation analysis and applications in biophotonics,” *Opt. Express***, 19**, 18871-18884, 2011.
[Cla1962] R. Clark Jones, “Information capacity of a beam of light,” *J. Opt. Soc. Am.***, 52**, 493-501, 1962.
[Col2007] C. P. Colvero, M. C. R. Cordeiro, and J. P. von der Weid, “FSO systems: Rain, drizzle, fog and haze attenuation at different optical windows propagation,” Microwave and Optoelectronics Conference, 2007. IMOC 2007. SBMO/IEEE MTT-S International, pp. 563–568, IEEE, 2007.
[Cov2006] T. M. Cover and J. A. Thomas, *Elements of Information Theory*, 2nd Ed., John Wiley & Sons, Hoboken NJ, 2006.
[Cui2010a] M. Cui, E. J. McDowell, and C. Yang, "An *in vivo* study of turbidity suppression by optical phase conjugation (TSOPC) on rabbit ear," *Opt. Express*, **18**, 25–30, 2010.
[Cui2010b] M. Cui and C. Yang, “Implementation of a digital optical phase conjugation system and its application to study the robustness of turbidity suppression by phase conjugation”, *Optics Express*, **18**, 3444-55, 2010.
[Dai1975] J.C. Dainty, *Laser Speckle and Related Phenomena*, Springer, Berlin 1975.
[Dam2011] G. M. van Dam, G. Themelis, L. M. A. Crane, N. J. Harlaar, R. G. Pleijhuis, W. Kelder, A. Sarantopoulos, J. S. de Jong, H. J. G. Arts, A. G. J. van der Zee, J. Bart, P. S. Low, and V. Ntziachristos, “Intraoperative tumor-specific fluorescence imaging in ovarian cancer by folate receptor-a targeting: first in-human results,” *Nature Medicine*, **17**, 1315-1319, 2011.
[Dau1992] I. Daubechies, *Ten Lectures on Wavelets*, SIAM, 1992.
[Dav2012] M.A. Davenport, M.F. Duarte, Y.C. Eldar, and G. Kutyniok, *Introduction to Compressed Sensing*, in *Compressed Sensing: Theory and Applications*, Eds. Y.C. Eldar, and G. Kutyniok, Cambridge University Press, 2012.
[DiL2011] R. Di Leonardo and S. Bianchi, “Hologram transmission through multi-mode optical fibers,” *Opt. Express*, **19** , 247-254, 2011.
[Don2006] D. L. Donoho, “Compressed sensing,” *IEEE Trans. Inf. Theory*, **52**, 1289-1306, 2006.
[Dor1984] O. N. Dorokhov, “On the coexistence of localized and extended electronic states in the metallic phase,”

Solid State Communications, **51**, 381-384, 1984.
[Dow1993] C. D. O'Dowd and M. H. Smith, "Physicochemical properties of aerosols over the northeast Atlantic: Evidence for windspeed-related submicron sea-salt aerosol production," *J. Geophys. Res.-Atmos.*, 1993.
[Dre2001] W. Drexler, U. Morgner, R. K. Ghanta, F. X. Kärtner, J. S. Schuman, and J. G. Fujimoto, *Nat. Med.*, **7**, 502-507, 2001.
[Dua2008] M. F. Duarte, M. A. Davenport, D. Takhar, J. N. Laska, T. Sun, K. F. Kelly, and R. G. Baraniuk, "Single-pixel imaging via compressive sampling," *IEEE Signal Process. Mag.*, **25**, 83-91, 2008.
[Dur2004] T. Durduran, G. Yu, M. G. Burnett, J. a. Detre, J. H. Greenberg, J. Wang, C. Zhou, and A. G. Yodh, "Diffuse optical measurement of blood flow, blood oxygenation, and metabolism in a human brain during sensorimotor cortex activation," *Opt. Lett.*, **29**, 1766, 2004.
[Dur2010] T. Durduran, R. Choe, W. B. Baker, and A. G. Yodh, "Diffuse optics for tissue monitoring and tomography," *Rep. Prog. Phys.*, **73**, 076701, 2010.
[Fan2008] Q. Fang, S. A. Carp, J. Selb, G. Boverman, Q. Zhang, D. B. Kopans, R. H. Moore, E. L. Miller, D. H. Brooks, and D. A. Boas, "Combined optical imaging and mammography of the healthy breast: optical contrast derived from breast structure and compression," *IEEE Trans. Med. Imag.* **28**, 30–42 (2008).
[Fen1988] S. Feng, C. Kane, P. A. Lee, and A. D. Stone, "Correlations and fluctuations of coherent wave transmission through disordered media," *Phys. Rev. Lett.*, **61**, 834-837, 1988.
[Fre1990] I. Freund, "Looking through walls and around corners," *Physica A*, **168**, 49, 1990.
[Fio2012] R. Fiolka, K. Si, and M. Cui, "Complex wavefront corrections for deep tissue focusing using low coherence backscattered light," *Optics Express*, **20**, 16532, 2012.
[För1948] T. Förster, "Zwischenmolekulare energiewanderung und fluoreszenze," *Ann. Physik* **2**, 55 (1948).
[Gab1946] D. Gabor, "Theory of communication. Part 1: The analysis of information," *J. Inst. Radio and Comm. Eng.*, **93**, 429-441, 1946.
[Gai2009] V. Gaind, K. J. Webb, S. Kularatne, and C. A. Bouman, "Towards *in vivo* imaging of intramolecular fluorescence resonance energy transfer parameters," *J. Opt. Soc. Am. A* **26**, 1805–1813 (2009).
[Gai2010] V. Gaind, S. Kularatne, P. Low, and K. J. Webb, "Deep tissue imaging of intramolecular fluorescence resonance energy transfer parameters," *Opt. Lett.* **35**, 1314–1316 (2010).
[Gib2005] A. P. Gibson, J. C. Hebden, and S. R. Arridge, "Recent advances in diffuse optical imaging," *Phys. Med. Biol.*, **50**, R1–43, 2005.
[Gig2012] S. Gigan, Endoscopy slims down, *Physics*, **5**, 127, 2012.
[Gjo2013] B. Gjonaj, J. Aulbach, P. M. Johnson, A. P. Mosk, L. Kuipers, and A. Lagendijk, "Focusing and scanning microscopy with propagating surface plasmons," *Phys. Rev. Lett.*, **110**, 266804: 1-5, 2013.
[Goe2013] A. Goetschy and A. D. *Stone, Filtering Random Matrices: The Effect of Incomplete Channel Control in Multiple Scattering, Phys. Rev. Lett.*, **111**, 063901, 2013.
[Goo2007] J. W. Goodman, *Speckle Phenomena in Optics: Theory and Applications*, Roberts & Co., Englewood CO, 2007.
[Gra2003] E. E. Graves, J. Ripoll, R. Weissleder, and V. Ntziachristos, "A submillimeter resolution fluorescence molecular imaging system for small animal imaging," *Med. Phys.*, **30**, 901-911, 2003.
[Gup2012] O. Gupta, T. Willwacher, A. Velten, A. Veeraraghavan, and R. Raskar, "Reconstruction of hidden 3D shapes using diffuse reflections," *Optics Express*, **20**, 19096, 2012.
[Hao2014] X. Hao, L. Martin-Rouault, and M. Cui, "A self-adaptive method for creating high efficiency communication channels through random scattering media," *Sci. Rep.*, **4**, 2014.
[Har1998] J. W. Hardy, *Adaptive Optics for Astronomical Telescopes, Oxford University Press*, 1998.
[Hel2005] F. Helmchen and W. Denk, "Deep tissue two-photon microscopy," *Nat. Methods*, **2**, 932-940, 2005.
[Hin2012] W. C. Hinds, *Aerosol Technology, Properties, Behavior, and Measurement of Airborne Particles*, John Wiley & Sons, 2012.
[Hop1990] W. A. Hoppel, J. W. Fitzgerald, G. M. Frick, R. E. Larson, and E. J. Mack, "Aerosol size distributions and optical properties found in the marine boundary layer over the Atlantic Ocean," *J. Geophys. Res.-Atmos.*, **95**, 3659–3686, 1990.
[Hor2013] N. G. Horton, K. Wang, D. Kobat, C. G. Clark, F. W. Wise, C. B. Schaffer, and C. Xu, "*In vivo* three-photon microscopy of subcortical structures within an intact mouse brain," *Nature Photon*, **7**, 205 – 209, 2013.
[Hou1949] H. G. Houghton and W. R. Chalker, "The scattering cross section of water drops in air for visible light," *J. Opt. Soc. Am.*, **39,** 955–955, 1949.
[Hsi2010] C. Hsieh, Y. Pu, R. Grange, G. Laporte, and D. Psaltis, "Imaging through turbid layers by scanning the phase conjugated second harmonic radiation from a nanoparticle," *Opt. Express*, **18**, 20723-20731, 2010.

[Hua1991] D. Huang, E. A. Swanson, C. P. Lin, J. S. Schuman, W. G. Stinson, W. Chang, M. R. Hee, T. Flotte, K. Gregory, and C. A. Puliafito, "Optical coherence tomography," *Science*, **254**, 1178-1181, 1991.
[Hun2013] J. Hunt, T. Driscoll, A. Mrozack, G. Lipworth, M. Reynolds, D. Brady, and D. R. Smith, "Metamaterial Apertures for Computational Imaging," *Science*, **339**, 310 – 313, 2013.
[Ish1978] A. Ishimaru, *Wave Propagation and Scattering in Random Media*, Academic Press, 1978.
[Jan2013] J. Jang, J. Lim, H. Yu, H. Choi, J. Ha, J.-H. Park, W.-Y. Oh, W. Jang, S. Lee, and Y. Park, "Complex wavefront shaping for optimal depth-selective focusing in optical coherence tomography," *Optics Expr.*, **21**, 2890-2902, 2013.
[Jan2014] H. Jang, C. Yoon, E. Chung, W. Choi, and H.-N. Lee, "Speckle suppression via sparse representation for wide-field imaging through turbid media," *Optics Express*, **22**, 16619, 2014.
[Jan2015] M. Jang, H. Ruan, I. M. Vellekoop, B. Judkewitz, E. Chung, and C. Yang, "Relation between speckle decorrelation and optical phase conjugation (OPC)-based turbidity suppression through dynamic scattering media: a study on in vivo mouse skin," *Biomed. Opt. Express* **6,** 72, 2015.
[Jud2013] B. Judkewitz, Y. M. Wang, R. Horstmeyer, A. Mathy, and C. Yang, "Speckle-scale focusing in the diffusive regime with time reversal of variance-encoded light (TROVE)," *Nature Photon.*, **7**, 300-305, 2013.
[Jud2015] B. Judkewitz, R. Horstmeyer, I.M. Vellekoop, I. Papadopoulos, and C. Yang, "Translation correlations in anisotropically scattering media," *Nature Physics* **11**, 684-689 (2015).
[Kat2009] O. Katz, Y. Bromberg and Y Silberberg, "Compressive ghost imaging," *Appl. Phys. Lett.*, 95, 131110, 2009.
[Kat2011] O. Katz, E. Small, Y. Bromberg, and Y. Silberberg, "Focusing and compression of ultrashort pulses through scattering media," *Nature Photonics***,** **5**, 372-377, 2011.
[Kat2012] O. Katz, E. Small, and Y. Silberberg, "Looking around corners and through thin turbid layers in real time with scattered incoherent light," *Nature Photon.*, **6**, 549-553, 2012.
[Kat2014a] O. Katz, P. Heidmann, M. Fink, and S. Gigan, "Non-invasive real-time imaging through scattering layers and around corners via speckle correlations," *arXiv preprint* 1403.3316, 2014.
[Kat2014b] O. Katz, E. Small, Y. Bromberg and Y. Silberberg, *Optica* 1, 170, 2014.
[Kim2012] M. Kim, Y. Choi, C. Yoon, W. Choi, J. Kim, Q.-H. Park, and W. Choi, "Maximal energy transport through disordered media with the implementation of transmission eigenchannels," *Nature Photonics*, **6**, 581-585, 2012.
[Lai2011] P. Lai, X. Xu, H. Liu, Y. Suzuki, and L. V. Wang, "Reflection-mode time-reversed ultrasonically encoded optical focusing into turbid media," *J. Biomed. Opt.*, **16**, 080505, 2011.
[Li1994] J. Li and A. Genack, "Correlation in laser speckle," *Physical Review E*, **49**, 4530, 1994.
[Lie2014] S. F. Liew, S. M. Popoff, A. P. Mosk, W. L. Vos, and H. Cao, "Transmission channels for light in absorbing random media: from diffusive to ballistic-like transport," *Phys. Rev. B*, **89**, 224202: 1-10, 2014.
[Liu2014] A. Liutkus, D. Martina, S. Popoff, G. Chardon, O. Katz, G. Lerosey, S. Gigan, L. Daudet, and I. Carron, "Imaging with nature: compressive imaging using a multiply scattering medium,"*Sci. Rep.*, **4**, 5552, 2014.
[Ma2014] C. Ma, X. Xu, Y. Liu, and L. V. Wang, "Time-reversed adapted-perturbation (TRAP) optical focusing onto dynamic objects inside scattering media," *Nat. Photonics* **8,** 931–936, 2014.
[Mac1989] F. MacKintosh and S. John, "Diffusing-wave spectroscopy and multiple scattering of light in correlated random media," *Phys. Rev. B* **40**, 2383–2406, 1989.
[Mah2013] R. N. Mahalati, R. Y. Gu, and J. M. Kahn, "Resolution limits for imaging through multi-mode fiber," *Opt. Express*, **21**, 1656-1668, 2013.
[Mar1967] V. A. Marcenko and L. A. Pastur, "Distribution of eigenvalues for some sets of random matrices," *Mathematics of the USSR-Sbornik* **1**(4), 457-483, 1967.
[Mar1987] G. Maret and P. Wolf, "Multiple light scattering from disordered media. The effect of Brownian motion of scatterers," *Zeitschrift für Phys. B Condens. Matter* **413**, 409–413, 1987.
[Mau2011]cC. Maurer, A. Jesacher, S. Bernet, and M. Ritsch-Marte, "What spatial light modulators can do for optical microscopy," *Laser & Photon. Rev.***,** **5**, 81-101, 2011.
[McC2011] D. McCabe, A. Tajalli, D. Austin, P. Bondareff, I. Walmsley, S. Gigan, and B. Chatel, "Spatio-temporal focusing of an ultrafast pulse through a multiply scattering medium," *Nat. Commun.*, **2**, 447, 2011.
[Mck2000] J. D.McKinney, M. A.Webster, K. J.Webb, and A.M.Weiner, "Characterization and maging in optically scattering media by use of laser speckle and a variable-coherence source," *Opt. Lett.*, **25,** 4–6, 2000.
[McK2004] D. MacKay, *Information Theory, Inference, and Learning Algorithms*, Cambridge University Press, 3rd ed., 2004
[Mel1988] P. A. Mello, P. Pereyra, and N. Kumar, "Macroscopic approach to multichannel disordered conductors," *Ann. Phys.*, **181**, 290-317, 1988.

[Mel1994] I. N. Mel'Nikova and V. V. Mikhaylov, "Spectral scattering and absorption coefficients in strati derived from aircraft measurements," *J. Geophys. Res.-Atmos.*, **51**, 925–931, 1994.
[Mel2001] I. N. Mel'Nikova and V. V. Mikhailov, "Vertical profiles of stratus cloud spectral optical parameters derived from airborne radiation measurements," *J. Geophys. Res.-Atmos.*, **106**, 27465–27471, 2001.
[Mil2002] A. B. Milstein, S. Oh, J. S. Reynolds, K. J. Webb, C. A. Bouman, and R. P. Millane, "Three-dimensional Bayesian optical diffusion imaging using experimental data," *Opt. Lett*. **27,** 95–97, 2002.
[Mil2004] A. B. Milstein, J. J. Stott, S. Oh, D. A. Boas, R. P. Millane, C. A. Bouman, and K. J. Webb, "Fluorescence optical diffusion tomography using multiple-frequency data," *J. Opt. Soc. Am. A* **21,** 1035–1049, 2004.
[Mil2005b] A. B. Milstein, M. D. Kennedy, P. S. Low, C. A. Bouman, and K. J. Webb, "Detection and localization of a fluorescent mouse tumor in a turbid medium," *Appl. Opt.* **44,** 2300–2310, 2005.
[Mos2012] A. P. Mosk, A. Lagendijk, G. Lerosey, and M. Fink, "Review: Controlling waves in space and time for imaging and focusing in complex media," *Nature Photon.*, **6**, 283-292, 2012.
[Mou2000] A. L. Moustakas, H. U. Baranger, L. Balents, A. M. Sengupta, and S. H. Simon, *Science 287*, **287**, 2000.
[Nai2014] N. Naik, C. Barsi, A. Velten, and R. Raskar, "Estimating wide-angle, spatially varying reflectance using time-resolved inversion of backscattered light," *Journal of the Optical Society of America A,* **31**, 957, 2014.
[Nas2004] N. Nassif, B. Cense, B. H. Park, S. H. Yun, T. C. Chen, B. E. Bouma, G. J. Tearney, and J. F. de Boer, "*In vivo* human retinal imaging by ultrahigh-speed spectral domain optical coherence tomography," *Opt. Lett.*, **29**, 480-482, 2004.
[New2012] J. A. Newman and K. J. Webb, "Fourier magnitude of the field incident on a random scattering medium from spatial speckle intensity correlations," *Opt. Lett*. **37,** 1136–1138, 2012.
[New2014b] J. A. Newman and K. J. Webb, "Imaging optical fields through heavily scattering media," *Phys. Rev. Lett.,* **113**, 263903, 2014.
[Nix2013] M. Nixon, O. Katz, E. Small, Y. Bromberg, A. A. Friesem, Y. Silberberg and N. Davidson, "Real-time wavefront shaping through scattering media by all-optical feedback," *Nature Photonics* **7**, 919–924, 2013.
[Ntz2006] V. Ntziachristos, Fluorescence molecular imaging, *Annu. Rev. Biomed. Eng.*, **8**, 1-33, 2006.
[Ntz2010] V. Ntziachristos, "Going deeper than microscopy: the optical imaging frontier in biology," *Nature Methods*, **7**, 603-614, 2010.
[Oh2002] S. Oh, A. B. Milstein, R. P. Millane, C. A. Bouman, and K. J. Webb, "Source-detector calibration in three-dimensional Bayesian optical diffusion tomography," *J. Opt. Soc. Am. A*, **19,** 1983–1993, 2002.
[Oh2005] S. Oh, A. B. Milstein, C. A. Bouman, and K. J. Webb, "A general framework for nonlinear multigrid inversion," *IEEE Trans. on Image Process*. **14,** 125–140, 2005.
[Out1993] P.N. den Outer, Th.M. Nieuwenhuizen, and A. Lagendijk, "Location of objects in multiple-scattering media," *J. Opt. Soc. Am. A***, 10**, 1209, 1993.
[Pap2002] R. Pappu, B. Recht, J. Taylor, and N. Gershenfeld, *Science* **297**, 2026, 2002.
[Pap2013] I. N. Papadopoulos, S. Farahi, C. Moser, and D. Psaltis, "High-resolution, lensless endoscope based on digital scanning through a multimodeoptical fiber,"*Biomed. Opt. Express*, **4**, 260-270, 2013.
[Par2013] J.-H. Park, C. Park, H..S. Yu, J. Park, S. Han, J. Shin, S. H. Ko, K. T. Nam, Y.-H. Cho, and Y. K. Park, "Subwavelength light focusing using random nanoparticles," *Nature Photon.***, 7**, 454–458, 2013.
[Pen1983] J. B. Pendry, "Quantum limits to the flow of information and entropy," *J. Phys. A*, **16**, 2161, 1983.
[Pen1990] J. Pendry, A. MacKinnon, and A. Pretre, "Maximal fluctuations -- A new phenomenon in disordered systems," *Physica A*, **168**, 400-407, 1990.
[Pen2008] J. B. Pendry, "Light finds a way through the maze," *Physics*,**1**, 20, 2008.
[Pin1988] D. Pine, D. Weitz, P. Chaikin, and E. Herbolzheimer, "Diffusing wave spectroscopy," *Phys. Rev. Lett.* **60**, 1988.
[Pop2000] G. Popescu and A. Dogariu, "Ballistic attenuation of low-coherence fields," *Appl. Optics*, **39**, 4469, 2000.
[Pop2010] S. Popoff, G. Lerosey, R. Carminati, M. Fink, A. Boccara, and S. Gigan, "Measuring the transmission matrix in optics: An approach to the study and control of light propagation in disordered media," *Phys. Rev. Lett*, **104**, 100601, 2010.
[Pop2010b] Popescu G., Ed., *Nanobiophotonics*, McGraw-Hill, New York, 2010.
[Put2011] E. G. van Putten, D. Akbulut, J. Bertolotti, W. L. Vos, A. Lagendijk, and A. P. Mosk,"Scattering Lens Resolves sub-100 nm Structures with Visible Light," *Phys. Rev. Lett.,*. **106**, 193905: 1-4, 2011.
[Put2012] E. G. van Putten, A. Lagendijk, and A. P. Mosk , "Non-imaging speckle interferometry for high speed nanometer-scale position detection," *Opt. Lett.*, **37**, 1070-1072, 2012.
[Rey1996] J. S. Reynolds, A. Przadka, S. Yeung, and K. J. Webb, "Optical diffusion imaging: a comparative

numerical and experimental study," *Appl. Opt*. **35,** 3671–3679, 1996.
[Rip1999] J. Ripoll, M. N. Vesperinas, and R. Carminati, "Spatial resolution of diffuse photon density waves," *J. Opt. Soc. Am. A*, **16**(6), 1466-1476, 1999.
[Rua2014] H. Ruan, M. Jang, B. Judkewitz, and C. Yang, "Iterative time-reversed ultrasonically encoded light focusing in backscattering mode," *Sci. Rep.* **4,** 7156, 2014.
[Rue2006] M. Rueckel, J. A. Mack-Bucher, and W. Denk, "Adaptive wavefront correction in two-photon microscopy using coherence-gated wavefront sensing," *Proc. Nat. Acad. Sc*. **103**, 17137 – 17142, 2006.
[Seb2001] P. Sebbah (Ed.), *Waves and Imaging Through Complex Media*, Kluwer Academic, Dordrecht, Netherlands, 2001.
[She2010b] https://www.dri.edu/images/stories/editors/leapfrog/techprog/IIIa_5_Sheng.pdf
[Shi2012] Z. Shi and A. Z. Genack, "Transmission eigenvalues and the bare conductance in the crossover to Anderson localization," *Phys. Rev. Lett.* **108**, 043901, 2012.
[Si2012] K. Si, R. Fiolka, and M. Cui, "Fluorescence imaging beyond the ballistic regime by ultrasound-pulse-guided digital phase conjugation," *Nature Photon.* **6** , 657, 2012.
[Sim2013] R. D. Simmonds and M. J. Booth, "Modelling of multi-conjugate adaptive optics for spatially variant aberrations in microscopy," *J. Opt.* **15**, 094010, 2013.
[Sve2013] T. Svensson, R. Savo, E. Alerstam, K. Vynck, M. Burresi, and D. S. Wiersma, "Exploiting breakdown of the similarity relation for diffuse light transport: simultaneous retrieval of scattering anisotropy and diffusion constant," *Optics Letters* **38**, 437-439, 2013.
[Taj2014] E. Tajahuerce, V. Durán, P. Clemente, E. Irles, F. Soldevila, P. Andrés, and J. Lancis, "Image transmission through dynamic scattering media by single-pixel photodetection," *Optics Express* **22**, 16945, 2014.
[Tan1997] D. Tanr´e, Y. J. Kaufman, and M. Herman, "Remote sensing of aerosol properties over oceans using the MODIS/EOS spectral radiances," *J. Geophys. Res.-Atmos.*, 1997.
[Tuc2007] V.V. Tuchin, *Tissue Optics: Light Scattering Methods and Instruments for Medical Diagnosis*, Second ed., SPIE Press, 2007.
[Tur2005] G. M. Turner, G. Zacharakis, A. Soubret, J. Ripoll, and V. Ntziachristos, "Complete-angle projection diffuse optical tomography by use of early photons," *Optics Letters* **30**, 409, 2005.
[Tul2004] A. M. Tulino and S. Verdu, *Random Matrix Theory and Wireless Communications*, Edn. 2nd. Now Publishers Inc; 2004.
[Tys2010] R. K. Tyson, *Principles of Adaptive Optics, 3rd ed.*, (CRC Press, Boca Raton, 2010.
[Vel2007] I. M. Vellekoop and A. P. Mosk, "Focusing coherent light through opaque strongly scattering media," *Opt. Lett.* **32**, 2309-2311 (2007).
[Vel2008a] I.M. Vellekoop and A.P. Mosk, "Universal optimal transmission of light through disordered materials," *Phys. Rev. Lett.* **101**, 120601: 1-4 (2008).
[Vel2008b] I. M. Vellekoop, E.G. van Putten, A. Lagendijk and A. P. Mosk, "Demixing light paths in disordered metamaterials," *Opt. Express* **16**, 67-80 (2008).
[Vel2010a] I.M. Vellekoop, A. Lagendijk, and A. P. Mosk, "Exploiting disorder for perfect focusing," *Nature Photon.* **4**, 320 - 322 (2010).
[Vel2012] I. M. Vellekoop, M. Cui, and C. Yang, "Digital optical phase conjugation of fluorescence in turbid tissue," *Appl. Phys. Lett.* **101**, 081108 (2012).
[Wan1991] L. Wang, P. Ho, C. Liu, G. Zhang, and R. Alfano, "Ballistic 2-d imaging through scattering walls using an ultrafast optical Kerr gate," *Science* **253**, 769 (1991).
[Wan2006] Z. Wang, M. A. Webster, A. M. Weiner, and K. J. Webb, "Polarized temporal impulse response for scattering media from third-order frequency correlations of speckle intensity patterns," *J. Opt. Soc. Am. A* **23,** 3045–3053, 2006.
[Wan2007a] L. V. Wang, and H.-i. Wu, *Biomedical Optics: Principles and Imaging*, (Wiley, Hoboken NJ, 2007).
[Wan2010] Z. Wang, K. Webb, and A. Weiner, "Coherent incident field information through thick random scattering media from speckle correlations over source position," *Appl. Opt* **49**, 5899-5905 (2010).
[Wan2012b] Y. Wang, B. Judkewitz, C. DiMarzio, and C. Yang, "Deep-tissue focal fluorescence imaging with digitally time-reversed ultrasound-encoded light," *Nature Communications* **3**, 928, 2012.
[Web2000] M. A. Webster, K. J. Webb, and A. M. Weiner, "Temporal response of a random medium from laser speckle frequency correlations," *Phys. Rev. Lett.* **88,** 033901, 2002.
[Web2004] M. A. Webster, T. D. Gerke, A. M. Weiner, and K. J. Webb, "Spectral and temporal speckle field measurements of a random medium," *Opt. Lett.* **29**, 1491, 2004.
[Wel1977] W. C. Wells, G. Gal, and M. W. Munn, "Aerosol distributions in maritime air and predicted scattering coefficients in the infrared," *Appl. Opt*., 1977.

[Whi2010] B. R. White and J. P. Culver, “Quantitative evaluation of high-density diffuse optical tomography: *in vivo* resolution and mapping performance,” *Journal of Biomedical Optics*, **15**(2), 026006, 2010.
[Wie2013] D. S. Wiersma, “Disordered photonics,” *Nature Photonics*, **7**, 188-196, 2013.
[Wu2014] X. Wu, A. T. Eggebrecht, S. L Ferradal, J. P. Culver, and H. Dehghani, “Quantitative evaluation of atlas-based high-density diffuse optical tomography for imaging of the human visual cortex,” *Biomedical Optics Express*, **5**(11), 3882-3900, 2014.
[Xu2011] X. Xu, H. Liu, and L. Wang, “Time-reversed ultrasonically encoded optical focusing into scattering media,” *Nature Phot.* **5** , 154-157, 2011.
[Xux2011] X. Xu, H. Liu, and L. V. Wang, “Time-reversed ultrasonically encoded optical focusing into scattering media,” *Nat. Photonics* **5**, 154–157, 2011.
[Yan2014] X. Yang, Y. Pu, and D. Psaltis, “Imaging blood cells through scattering biological tissue using speckle scanning microscopy,” *Optics Express* **22**, 3405, 2014.
[Ye1999a] J. C. Ye, K. J. Webb, C. A. Bouman, and R. P. Millane, “Optical diffusion tomography using iterative coordinate descent optimization in a Bayesian framework,*” J. Opt. Soc. A* **16,** 2400–2412, 1999.
[Ye1999b] J. C. Ye, K. J. Webb, R. P. Millane, and T. J. Downar, “Modified distorted Born iterative method with an approximate Fréchet derivative for optical diffusion tomography,” *J. Opt. Soc. Am. A* **16,** 1814–1826, 1999.
[Ye2001] J. C. Ye, C. A. Bouman, K. J. Webb, and R. P. Millane, “Nonlinear multigrid algorithms for Bayesian optical diffusion tomography,” *IEEE Trans. Image Proc.* **10,** 909–922, 2001.
[Yil2013] H. Yilmaz, W. L. Vos, and A. P. Mosk, “Optimal control of light propagation through multiple-scattering media in the presence of noise,*” Biomed. Opt. Express***,** **4**, 1759-1768, 2013.
[Yod1995] A. Yodh, and B. Chance, “Spectrocopy and imaging with diffusing light,” *Phys. Today*, **48**, 34-40, 1995.
[Yu2013] H. Yu, T. R. Hillman, W. Choi, J. O. Lee, M. S. Feld, R. R. Dasari, and Y. Park, “Measuring large optical transmission matrices of disordered media,” *Physical Review Letters*, **111**, 153902, 2013.
[Zac2006] G. Zacharakis, H. Shih, J. Ripoll, R. Weissleder, and V. Ntziachristos, “Normalized transillumination of fluorescent proteins in small animals,” *Molecular imaging*, **5**, 153-159, 2006.
[Zef2007] B. W. Zeff, B. R. White, H. Dehghani, B. L. Schlaggar, and J. P. Culver, “Retinotopic mapping of adult human visual cortex with high-density diffuse optical tomography,” *Proceedings of the National Academy of Sciences*, **104**(29), 12169-12174, 2007.
[Zer1938] F. Zernike, “The concept of degree of coherence and its application to optical problems,” *Physica*, **5**, 785-795, 1938.
[Zho2014a] E. H. Zhou, H. Ruan, C. Yang, and B. Judkewitz, "Focusing on moving targets through scattering samples," *Optica* **1,** 227, 2014.